

Data imputation Neural network modelling to estimate particle size distribution based on other particle sections and meteorological parameters in situ measured particle size distributions by means of neural networks

Pak Lun Fung^{1,2}, Martha Arbayani Zaidan^{1,3}, Ola Surakhi⁴, Sasu Tarkoma⁵, Tuukka Petäjä^{1,3} and Tareq Hussein^{1,6,7}

¹Institute for Atmospheric and Earth System Research / Physics, Faculty of Science, University of Helsinki, Finland; pak.fung@helsinki.fi; martha.zaidan@helsinki.fi; tuukka.petaja@helsinki.fi; tareq.hussein@helsinki.fi

²Helsinki Institute of Sustainability Science, Faculty of Science, University of Helsinki, Finland

³Joint International Research Laboratory of Atmospheric and Earth System Sciences, School of Atmospheric Sciences, Nanjing University, Nanjing 210023, China

⁴Department of Computer Science, The University of Jordan, Amman 11942, Jordan; ola.surakhi@gmail.com

⁵Department of Computer Science, Faculty of Science, University of Helsinki, Finland; sasu.tarkoma@helsinki.fi

⁶Department Material Analysis and Indoor Chemistry, Fraunhofer WKI, D-38108 Braunschweig, Germany

⁷Department of Physics, The University of Jordan, Amman 11942, Jordan

Correspondence to: Pak Lun Fung and Tareq Hussein

Abstract.

In air quality research, often only size-integrated particle mass concentrations as indicators of aerosol particles are considered. However, the mass concentrations do not provide sufficient information to convey the full story of fractionated size distribution, in which the particles of different diameters (D_p) are able to deposit differently on respiratory system and cause various harm. Aerosol size distribution measurements rely on a variety of techniques to classify the aerosol size and measure the size distribution. From the raw data the ambient size distribution is determined utilising a suite of inversion algorithms. However, the inversion problem is quite often ill-posed and challenging to solve/invert. Due to the instrumental insufficiency and inversion limitations, models-imputation methods for fractionated particle size distribution are of great significance to fill the missing gaps or negative values. The study at hand involves a merged particle size distribution, from a scanning mobility particle sizer (NanoSMPS) and an optical particle sizer (OPS) covering the aerosol size distributions from 0.01 to 0.42 μm (electrical mobility equivalent size) and 0.3 μm to 10 μm (optical equivalent size) and meteorological parameters collected at an urban background region in Amman, Jordan in the period of 1st Aug 2016–31st July 2017. We develop and evaluate feed-forward neural network (FFNN) models-approaches to estimate number concentrations at particular size bin with (1) meteorological parameters, (2) number concentration at other size bins, and (3) both of the above as input variables. Two layers with 10–15 neurons are found to be the optimal option. Lower-Worse model-performance is observed at the lower edge ($0.01 < D_p < 0.02 \mu\text{m}$), the mid-range region ($0.15 < D_p < 0.5 \mu\text{m}$) and the upper edge ($6 < D_p < 10 \mu\text{m}$). For the edges at both ends, the number of neighbouring size bins is limited and the detection efficiency by the corresponding instruments is lower compared to the other size bins. A distinct performance drop over the overlapping mid-range region is due to the deficiency of a merging algorithm. Another plausible reason for the poorer performance for finer particles is that they are more effectively removed from the atmosphere compared to the coarser particles so that the relationships between the input variables and the small particles is more dynamic. An observable overestimation is also found in early morning for ultrafine particles followed by a distinct underestimation before midday. In the winter, due to a possible sensor drift and interference artefacts, the model estimation performance is not as good as the other seasons. The FFNN approach model by meteorological parameters

Formatted: Subscript

Formatted: Subscript

Formatted: Subscript

Formatted: Subscript

41 using 5-min data ($R^2 = 0.22\text{--}0.58$) shows poorer results than data with longer time resolution ($R^2 = 0.66\text{--}0.77$). The [FFNN](#)
42 [approach](#) by the number concentration at the other size bins can serve as an alternative way to replace negative
43 numbers in size distribution raw dataset thanks to its high accuracy and reliability ($R^2 = 0.97\text{--}1$). This negative numbers
44 filling [approach](#) can maintain a symmetric distribution of errors [and complement the existing ill-posed built-in](#)
45 [algorithm in particle sizer instruments](#).

47 **Keywords.**

48 Aerosol size distribution, feed-forward neural network, atmospheric aerosols particles, missing data, SMPS, OPS

49 **1 Introduction**

50 Particulate matter (PM) is the principal component of air pollution. PM includes a range of particle sizes, such as coarse
51 ($1 < \text{particle diameter } (D_p) < 10 \mu\text{m}$), fine ($0.1 < D_p < 1 \mu\text{m}$), and ultrafine particles (UFP, $D_p < 0.1 \mu\text{m}$). Through human's
52 inhalation, coarse particles usually are partly deposited in the head airway ($5\text{--}30 \mu\text{m}$) by the inertial impaction mechanism,
53 and are partly deposited in the tracheobronchial region, mainly through sedimentation ($1\text{--}5 \mu\text{m}$). The particles may be
54 further absorbed or removed by mucociliary clearance (Gupta and Xie, 2018). The remaining fine and UFP, due to their
55 high surface area to mass ratios (Kreyling et al., 2004), penetrate deeply into the alveolar region, where removal
56 mechanisms may be insufficient (Gupta and Xie, 2018). Evidence suggests that the adverse associations of short-term
57 UFP exposure with acute and chronic problems ranging from inflammation, exacerbation of asthma, and metal fume fever
58 to fibrosis, chronic inflammatory lung diseases, and carcinogenesis (Spinazzè et al., 2017) might be at least partly
59 independent of other pollutants (Ohlwein et al., 2019). Various studies have demonstrated that inhaled or injected UFP
60 could enter systemic circulation and migrate to different organs and tissues (Londahl et al., 2014; Xing et al., 2016).

61 Other than health effects, particles of various sizes also contribute to Earth's ecosystem and climate differently. For
62 instance, fine and UFP are capable of growing up to diameters of $0.02\text{--}0.1 \mu\text{m}$ within a day (Kulmala et al., 2004;
63 Kerminen et al., 2018) where they constitute a fraction of cloud condensation nuclei, and thus, indirectly affecting the
64 climate (Kerminen et al., 2012). The drivers behind aerosol particles vary between natural and anthropogenic as well as
65 primary and secondary. Primary particles are emitted to the atmosphere as particles, such as sea salt or dust particles,
66 while secondary particles form in the atmosphere through gas-to-particle transformation, which has been known as new
67 particle formation (NPF) observed in various environments and contributing to a major fraction of the total particle
68 number budget (Kulmala et al., 2004; Kerminen et al., 2018). In addition, while fine particles cool the climate by
69 predominantly scattering shortwave radiation, coarse particles warm the climate system by absorbing both shortwave and
70 longwave radiation (Kok et al., 2017). Indeed, the complexity of urban aerosols is tribute to the fact that several sources
71 can contribute in the same particle size range (Rönkkö et al., 2017).

72
73
74 Currently, the most commonly reported aerosol variables are particle mass concentration and particle number
75 concentration. The former metric, which is dominated by coarser particles, is included as air quality indicators (e.g. mass
76 concentrations of both thoracic particles PM_{10} and fine particles $\text{PM}_{2.5}$); however, it has been argued that this might ignore
77 the potential adverse effect of UFP on health (Zhou et al., 2020). The latter one describes better the distribution of finer
78 particles, but it neglects the influence of coarse particles. Using either particle mass concentration or particle number
79 concentration solely is not enough to fully review the health effects and the Earth's climate system by aerosol particles.

Formatted: Subscript

Formatted: Subscript

Formatted: Subscript

80 Therefore, in order to understand the origin of atmospheric aerosol particles and their potential impacts at a specific
81 location, the whole size distribution of these particles needs to be studied (Zhou et al., 2020).

82
83 Recently, due to urbanization and increased population, megacities have increased their contribution to atmospheric
84 aerosol pollution massively (Lelieveld et al. (2015), Middle East and North Africa (MENA) regions, with an average
85 annual growth rate of 1.74% in 2019 (World Bank Group, 2019), has one of the world's regions most rapidly expanding
86 populations. With the population of 578 million, several cities in MENA regions are among the 20 most polluted cities in
87 the world. The annual average concentrations of some pollutants, for example PM_{2.5} in MENA (54.0 µg m⁻³) often exceed
88 5 times the WHO recommended levels (10.0 µg m⁻³) (World Health Organisation, 2019). Many countries in MENA are
89 dealing with negative impacts of air pollution in terms of both economic burden and health aspect (Ahmed et al., 2017;
90 Goudarzi et al., 2019). Air Pollution in this region is estimated to cause 133,000 premature deaths annually, almost half
91 of which are attributed to natural sources of air pollution, such as windblown sea salt and desert dust (Gherboudj et al.,
92 2017). Apart from natural pollutants, anthropogenic activities also play a major role in driving the air quality. They include
93 the extensive development of petrochemical industry, vehicular emissions and open burning of waste (Arhami et al.,
94 2018).

95
96 However, aerosol studies in this region have not paid attention to the aerosol number size distribution so far. Among the
97 few studies published, most report mass concentration (Goudarzi et al., 2019; Arhami et al., 2018; Borgie et al., 2016),
98 while some focused on the total particle number in MENA regions. Studies on the size-fractionated number concentrations
99 are, nonetheless, scarce (e.g. Hakala et al., 2019; Hakala et al., 2019) due to the unavailability of instruments for
100 measuring UFP in many air quality monitoring stations (Spinazzè et al., 2017). Determining aerosol number size
101 distribution for a wide size range in a reliable manner is a challenging task. The fact that the ambient distributions range
102 from nanometers to several micrometers dictates the use of multiple sizing techniques. For the sub-micron size range,
103 electrical mobility equivalent diameter is commonly used as the size parameter and the measurements are performed with
104 Differential Mobility Particle Sizer (DMPS) or Scanning Mobility Particle Sizer (SMPS) instruments (e.g. Wiedensohler
105 et al., 2012; Wiedensohler et al., 2012). These systems determine the aerosol size according to electrical mobility
106 equivalent size. The larger particles (approximately > 0.3 µm) can be classified according to their aerodynamic or optical
107 size (Kulkarni et al., 2011). In order to obtain the full aerosol size distribution, this data needs to be merged. Unfortunately
108 this task is not trivial as the merging requires knowledge on the chemical composition (influencing the refractive index
109 and thus the optical size), shape (influencing electrical mobility equivalent size), or effective density (influencing
110 aerodynamic size) (Kannosto et al., 2008).

111
112 In addition, the raw data from these instruments must be inverted to obtain the particle size distribution. This is not a
113 straightforward problem. A proper inversion algorithm is required to restore the particle size distribution from the raw
114 response (Cai et al., 2018) using the recorded kernel functions which describe the probability of particles of a
115 certain size being measured at a certain flow rate, influenced by the measured activation curves and the detection
116 efficiencies of the instruments (Lehtipalo et al., 2014) between the raw response and the size distribution (Cai et al., 2018).
117 Depending on the instruments used and the measurement environments, some use a built-in inversion algorithm in the
118 instruments, which replace negative raw values with artificial non-negative numbers. Some develop their own inversion
119 methods; however, they all have their drawbacks. Examples include that the least square method may magnify the random

Formatted: English (United Kingdom)

Formatted: English (United Kingdom)

Formatted: English (United Kingdom)

Formatted: English (United Kingdom)

120 errors in the raw counts in Condensation Particle Counter (CPC) raw counts into relatively large uncertainties (Enting
121 and Newsam, 1990), the stepwise method may cause non-negligible errors (Lehtipalo et al., 2014), and that the smoothing
122 step method may introduce bias in the shape of the inverted distribution function: (Markowski, 1987). Kandlikar and
123 Ramachandran (1999) pointed out that there is not a single universal inversion algorithm applicable to all situations.

124
125 In this study, the built-in inversion algorithm was used. Especially in the size range of low number concentration, This
126 algorithm can lead to negative values when the kernel functions are not optimally configured, especially in the size range
127 of low number concentration. These negative values have no physical meanings. Some experts in the in situ measurement
128 community might just omit the negative values or simply use nearest neighbour linear interpolation to replace the negative
129 values. However, the former method might cause asymmetric error for very small measured number concentration values
130 (Viskari et al., 2012), while the latter could result in too high values concurrently. To fill this knowledge gap, statistical
131 estimation model methods can serve as an alternative to estimate of size-fractioned number concentration by using other
132 available measurements.

133
134 Similar to other air quality parameters, modelling of size fractionated particle number concentrations have been
135 increasingly brought into the spotlight because of its potential health hazards. One of the most commonly used data-
136 driven methods, generalised linear regression models, have been extensively utilised in modelling size fractionated
137 particle number concentrations, for example, in urban regions in Helsinki, Finland Clifford et al., 2011; Hussein et al.,
138 2007, in Toronto, Canada Sabaliauskas et al., 2012, in Brisbane, Australia Rahman et al., 2017, and in three cities in
139 Germany Gerling et al., 2020. Besides linear regression models Mølgaard et al. (2013), refined the statistical model using
140 Bayesian inference and autoregressive parameters in five European cities Reggente et al. (2014) improvised by Gaussian
141 process based on the measurements of oxides of nitrogen in Antwerp, Belgium. These approaches are categorised as
142 transparent machine learning (ML) processes, as known as white box (WB) models, from which one can clearly explain
143 how they behave, how they produce predictions and what the influencing variables are Rudin, 2019. Another data driven
144 approach black box (BB) models, which refer to ML systems being viewed in terms of its inputs and outputs, without
145 any knowledge of its internal workings or underlying principles Rudin, 2019. They are considered to work generally
146 better in terms of accuracy, but provide limited transparency and accountability regarding the results Zaidan et al., 2019;
147 Fung et al., 2020. One example of BB model is artificial neural network (ANN), which were applied extensively to
148 estimate other air pollutant parameters Freeman et al., 2018; Cabaneros et al., 2019. They provide a robust approach for
149 approximating complex functions due to its ability to mimic non linearity of the functions and its well developed
150 optimisation. Al-Dabbous et al. (2017) has demonstrated the use of ANN to estimate three ranges of UPF at a roadside
151 site in Fahaheel, Kuwait. They addressed the importance of including meteorological parameters in the modelling process,
152 which was later validated by Zaidan et al. (2020) who estimated daily and hourly total particle number concentration by
153 only a combination of meteorological parameters in Amman, Jordan.

154
155 The-The main objectives of the paper is to estimate particleaerosol total-number concentration/ fill the negative values
156 making up for the shortcomings of the built-in inversion algorithm in particle sizer instruments. Extending from ~~from~~
157 meteorological observations and to advance the previous study by Zaidan et al. (2020), we build our imputation method
158 with a finer temporal and size-bin resolution. In order to do so, we place emphasis on to estimating particle number
159 concentration of a specific size bin by the interaction with other size bins and meteorological variables. In this study, we

Formatted: Highlight

Formatted: Highlight

Formatted: Highlight

Formatted: Highlight

Formatted: Highlight

Formatted: Highlight

Formatted: Highlight

Formatted: Highlight

Formatted: Highlight

Formatted: Highlight

Formatted: Highlight

Formatted: Highlight

Formatted: Highlight

Formatted: Highlight

Formatted: Highlight

Formatted: Highlight

Formatted: Highlight

Formatted: Highlight

Formatted: Highlight

Formatted: Highlight

Formatted: Highlight

Formatted: Highlight

Formatted: Highlight

Formatted: Highlight

Field Code Changed

Formatted: Not Highlight

160 propose three approaches in terms of different input variables ~~when we carry out the by means of neural~~
161 ~~networks modelling~~: (1) only meteorological parameters, (2) only particle size distribution, and (3) both particle size
162 distribution and meteorological parameters. Based on the general data analysis of the particle size distribution and the
163 meteorological condition, we ~~further~~ explain the source of different size bins at certain weather conditions and the
164 correlation among the particle size distribution and meteorological parameters in ~~Section 3~~. ~~We evaluate the proposed~~
165 ~~neural network method and compare it with other simpler methods in Sect. 4.1. Evaluation of models is discussed in~~
166 ~~Section 4~~. ~~In Sect. 4.2, we further discuss the temporal pattern of the proposed method~~ in terms of its diurnal cycle,
167 weekend effect and seasonal variation. ~~Besides, We also~~ examine the possible technical reasons for the pattern found
168 and the application of the ~~proposed method models~~.

169 2 Methods

170 2.1 Measurement sites and Instruments

171 In this study, we collected a dataset obtained from a measurement campaign in Amman, the capital city of Jordan, between
172 1 August 2016 and 31 July 2017. The city represents an area with Middle Eastern urban conditions within the Middle
173 East and North Africa (MENA) region. This region serves as a compilation of different aerosol particle sources including
174 natural dust, anthropogenic pollution (e.g., generated from the petrochemical industry and urbanization), as well as new
175 particle formation.

176
177 The database includes particle size distribution and meteorological parameters, as mentioned in the first step in Figure 1.
178 The aerosol measurement was carried out at the aerosol laboratory located on the third floor of the Department of Physics,
179 University of Jordan (32°00' N, 35°52' E) in the neighbourhood of Al Jubeiha. The campus is situated at an urban
180 background region in northern Amman. In particular, the campaign measured the particle number size distribution using
181 a scanning mobility particle sizer (NanoScan SMPS 3910, TSI, MN, USA) ~~with default settings~~. It monitors the particle
182 size distributions as electrical equivalent diameter 0.01–0.42 μm (13 channels). The size range of the SMPS system can
183 be extended to coarse particles with an additional compact instrument: an optical particle sizer (OPS 3330, TSI, MN,
184 USA). OPS measures optical diameter 0.3–10 μm (13 channels). This optical sizing method reports an optical particle
185 diameter, which is often different from the electrical mobility diameter measured by the SMPS technique. The
186 measurements were combined to provide a particle size distribution of wider particle diameter range 0.01–10 μm , which
187 is further described in ~~Section 2.2~~. The SMPS inlet ~~consists of copper tubing with a diffusion drier (TSI 3062-NC). The~~
188 ~~inlet~~ flow rate was 0.75 lpm ($\pm 20\%$) while the sample flow rate was 0.25 lpm ($\pm 10\%$). The flow rate of OPS was about 1
189 lpm. The aerosol transport efficiency ~~and losses~~ through the aerosol inlet assembly ~~and the diffusion drier~~ was determined
190 experimentally ~~in the laboratory~~: ambient aerosol sampling alternatively with and without sampling inlet, and the aerosol
191 data was corrected accordingly. The penetration efficiency was $\sim 47\%$ for 0.01 μm , $\sim 93\%$ for 0.3 μm and $\sim 40\%$ for 10
192 μm (Hussein et al., 2020). These deficiency of measurement at the upper and lower edges is somewhat in alignment with
193 other literatures. Particle size measured by nanoSMPS (Tritscher et al., 2013) tended to be underestimated for spherical
194 particles larger than 0.2 μm by up to 34% (Fonseca et al., 2016). Liu et al. (2014) clearly portrayed that the detection limit
195 of particle size below 0.03 μm is about 80–500 cm^{-3} , which is up to 10 times larger than that of coarser particles, for other
196 versions of SMPS. Stolzenburg and McMurry (2018) explained that discrepancies could be resulted from ~~Differential~~
197 ~~Mobility Analysers (DMAs)s~~ with transfer functions that were degraded (i.e., broadened) by flow distortions caused by

198 particle deposition within the classifier tube, sizing errors due to errors in flowmeter calibrations or leaks, CPC
199 concentration errors due to improper pulse counting, and continuity failure in the DMA high voltage connection.

200
201 The meteorological measurement was performed with a weather station (WH-1080, Clas Ohlson: Art.no.36-3242,
202 Helsinki, Finland) with a time resolution of 5 minutes. The meteorological data were comprised of ambient temperature
203 (Temp, resolution 0.1°C), relative humidity (RH, resolution 1%), wind speed (WS), wind direction (WD, 16 equal
204 divisions) and air pressure (P, resolution 0.3 hPa) (Hussein et al., 2019; Hussein et al., 2020; Zaidan et al., 2020). Wind
205 direction is resolved into north and east direction, as WD-N and WD-E, respectively. The data collection process is
206 illustrated in the first step in the database block in Figure 1.

207 **2.2 Data pre-processing**

208 The next step in [the database block in](#) Figure 1 is data pre-processing. Since the sampling time resolution of SMPS and
209 OPS was 1 min and 5 min, respectively, we synchronised the data into 5-min averages. Since a part of the size ranges in
210 both instruments are overlapping with each other, the last two size bins in SMPS and the first size bin in OPS were
211 neglected. Finally, we merged the size range of electrical mobility diameter 0.01–0.25 μm by SMPS and optical diameter
212 0.32–10 μm by OPS, and obtain a wider particle size distribution which covers the diameter range 0.01–10 μm . Merging
213 electrical mobility diameter and optical diameter can be a challenge and the overlapping region is often calculated with
214 high uncertainty (DeCarlo et al., 2004; Tritscher et al., 2015). The challenge arises because the optical diameters are
215 measured based on the refractive index of the particles, which depends on their chemical composition. Therefore, the
216 sizing will vary over time. There is also a ~~very~~ slight dependency with the SMPS system that is linked to the shape of the
217 particles, which influences their sizing.

218
219 We also calculated the particle number concentration with four particle diameter modes (size-fractionated number
220 concentration): nucleation (0.01–0.025 μm), Aitken (0.025–0.1 μm), accumulation (0.1–1 μm) and coarse mode (1–10
221 μm). Subsequently, the total number concentration was obtained as the sum of all these fractions. The size-fractionated
222 number concentrations were obtained by summing up the measured particle number size distribution over the specified
223 particle diameter range.

224
225 In order to perform [data imputation with](#) neural networks ~~modelling~~, aerosol and meteorological data were first linearly
226 interpolated [in time](#) in case of short missing data periods. For missing data over longer periods, the whole rows are
227 eliminated. The shorter missing data occurs due to technical faults while the longer missing periods are attributed to
228 instrument maintenance (Zaidan et al., 2020). Only 71.8% of total data was retained for [modelling the next step](#) in the
229 measurement period. Since the data were obtained from different measured variables with various physical units and
230 magnitudes, it was crucial to normalise the data. The scaling factor depends on which activation function is chosen. In
231 this case, the datasets were scaled so that it has a mean of 0 and a standard deviation of 1 to transform them into the range
232 of the activation function. The standardised data was then separated into different months for the reason of the seasonal
233 variation in the atmospheric condition. The data was further divided into training set (70%) and testing set (30%). The
234 processed data were also converted to hourly and daily averages for reporting purposes.

235 2.3 Setting of the neural network

236 After data collection and data pre-processing procedures, the next step is ~~method model~~ optimisation (Figure 1). ANN
237 models have been utilised in predicting air quality (Freeman et al., 2018; Maleki et al., 2019; Cabaneros et al., 2019;
238 Zaidan et al., 2020). Neural networks provide a robust approach for approximating real-valued target functions because
239 they can mimic the non-linearity of the functions and their optimization methods are well developed (Zaidan et al., 2017).
240 The architecture of neural networks consists of nodes as activation function (Figure 2), and the activation function in each
241 layer determines the output value of each neuron that becomes the input values for neurons in the next hidden layer
242 connected to it. In this paper, feed-forward neural network (FFNN) is used instead of a more sophisticated time delay
243 neural network (TDNN) because some of the rows in the dataset were removed in the data pre-processing step due to the
244 existence of missing data and TDNN cannot be performed without time continuity. FFNN usually consists of a series of
245 layers. The first layer has a connection from the network input. Each subsequent layer has a connection from the previous
246 layer. The final layer produces the network's output. A neuron can be thought as a combination of two parts:

$$z_j^{(L)} = \sigma\left(\sum_{i=1}^n w_{ji}^{(L)} x_i + b_j^{(L)}\right) \quad (1),$$

247 where $z_j^{(L)}$ and $b_j^{(L)}$ are the intermediate output and the bias term for the j^{th} neuron at L^{th} layer, respectively. $w_{ji}^{(L)}$ is the j^{th}
248 weight for each data points x_i at L^{th} layer. The second part performs the activation function (sigmoid function in this
249 study) on z_j to give out the output of the neuron:

$$\sigma(z_j^{(L)}) = \frac{1}{1 + \exp^{-z_j^{(L)}}} \quad (2),$$

250 The FFNN ~~method model~~ was created, trained and simulated with MATLAB (version: 8.3.0.532), using Neural Network
251 Toolbox. We initialised the weights randomly and the weights ~~were are~~ updated through ‘‘Levenberg-Marquardt’’
252 algorithm optimisation that was the fastest available back-propagation training function (Chaloulakou et al., 2003). We
253 performed several iterations within a cycle to minimise the training loss with Bayesian regularisation. These steps were
254 done iteratively until the best combination of the number of hidden layers and the corresponding number of neurons that
255 provided the minimum error was found. According to the review paper by Cabaneros et al. (2019), a shallow neural
256 network with one hidden layer and enough neurons in the hidden layers can fit any finite input-output mapping problem
257 for non-linear relationship. In the network training process, the number of neurons varied from 2 to 10 neurons per layer
258 with an incremental factor of 2 neurons in each simulation, and from 10 to 25 per layer with an incremental factor of 5
259 neurons in each simulation. To keep the ~~method model~~ simple, we consider only one or two layers in the simulation
260 process because the computing requirements could rise exponentially with the number of layers and neurons. Once we
261 pick the suitable ~~method model~~ configuration, the ~~method model~~ estimates number concentration using testing data.
262 Finally, the selected performance metrics, described in Section 2.4, can be calculated and we evaluate which approach is
263 the most suitable for size distribution estimation.

264 2.4 Other methods as comparison with the neural network method

265 In order to demonstrate the performance of the FFNN method, we perform similar procedures applying other simpler
266 methods, which have been widely used as means of data imputation (Junger and Ponce De Leon, 2015). They include
267 univariate and multivariate methods. The former includes unconditional mean (UM), median (MD), linear interpolation
268 (LinI), logarithmic interpolation (LogI), next neighbour interpolation (nNI) and previous neighbour interpolation (pNI).

where nNI was implemented as the next value carried backward while pNI as the previous value carried forward. The multivariate methods used in this study are conditional mean based on a linear regression of meteorological parameters and other particle size number concentrations as inputs (CM-met and CM-PSD, respectively). These methods are implemented as a comparison with the FFNN method.

2.5.4 Performance metrics

We choose the optimal combination of the number of hidden layers and the corresponding number of neurons by checking its mean absolute error (MAE), which is a simple way to illustrate the residuals of the estimated values by the estimation method. In order to identify which size bin manage to be predicted best, two metrics are used, namely coefficient of determination (R^2) and normalised root-mean-square error (NRMSE). R^2 measures how well the observed outcomes are replicated by the estimation method, based on the proportion of total variation of outcomes explained by the estimation method. NRMSE represents the standard deviation of the estimated errors with respect to its mean. NRMSE is used rather than commonly used RMSE because the number concentrations of the different size range are of different magnitudes. The comparison in different size range becomes different if RMSE is not normalised with its mean.

$$MAE = \frac{\sum_{i=1}^n |y_i - \hat{y}_i|}{n} \quad (3)$$

$$R^2 = 1 - \frac{\sum_{i=1}^n (y_i - \hat{y}_i)^2}{\sum_{i=1}^n (y_i - \bar{y})^2} \quad (4)$$

$$NRMSE = \frac{\sqrt{\frac{\sum_{i=1}^n (y_i - \hat{y}_i)^2}{n}}}{\bar{y}} \quad (5)$$

where y_i , \hat{y}_i and \bar{y} represent the i^{th} measurement value, the y^{th} estimated value by the estimation method and the mean of the all the measurement data, respectively. n notates the total number of the valid measurement data.

3 General data analysis

3.1 Environmental condition

Hussein et al. (2019) and Zaidan et al. (2020) investigated and described the effect of local weather conditions, respectively. Here we describe briefly the meteorological conditions during the measurement period as background information. Starting from August 2016, the daily temperature decreased gradually from 40°C to its tough 0°C in February 2017. It rose gradually to 40°C in August 2017. During the measurement period, the hourly median value was 19.9°C (Figure 3a). RH varied quite a lot from 10% to 100%, with an hourly median of 52.3%, and did not seem to have a seasonal pattern (Figure 3b). In summer months, wind appeared be stronger but the wind direction is more stable, mostly from northwest (270°–360°). In cold months, averaged wind speed was lower but wind blew from fluctuating direction. During the whole measurement period, wind speed ranged between 0–6 m s⁻¹ and its median is 1.39 m s⁻¹ (Figure 3c–d). Air pressure varied in a range from 892 to 912 hPa and its hourly median was 900 hPa In spite of the narrow range of variation, winter months seem to have slightly higher air pressure than summer months (Figure 3e).

Meteorological conditions have been suggested to influence particle number concentration. Hussein et al. (2019) demonstrated that number concentration had a rather complex relationship with temperature. Furthermore, number concentration of submicron had a decreasing trend with respect to the wind speed which indicates that most of the

Field Code Changed

Formatted: English (United States)

Formatted: English (United States)

Formatted: English (United States)

300 submicron fraction is originated from local sources such as combustion processes. Meanwhile, the number concentration
301 of coarse particles had higher concentrations at stagnant conditions and when the wind speed is higher than 5.5 m s^{-1} . It
302 is mainly because of road dust resuspension and might also be attributed to dust storm via long-range transport Hussein
303 et al., 2019). In this study, we further explore how wind direction influences the particle number concentration (Figure 4).
304 Wind coming from the northwest (225° – 325°) was generally stronger, but lower particle number concentration was
305 detected because the measurement area is at the outskirts of downtown. Wind from East and South (45° – 225°) has a lower
306 wind speed but a more intense hourly particle number concentration can be detected. From that direction situates the
307 urban city where all kinds of industrial activities take place. When considering only coarse particles, relatively high
308 number concentration is found when south-westerly wind is strong. This can further serve as an evidence that the source
309 of coarse particles in that region might come mostly from long range sea salt from Dead Sea or dust particles from nearby
310 deserts.

311 3.2 General pattern of particle size distribution

312 Hourly total number concentration ranged from $1.90 \times 10^3 \text{ cm}^{-3}$ to $1.52 \times 10^5 \text{ cm}^{-3}$ and its median was $1.36 \times 10^4 \text{ cm}^{-3}$. Figure
313 5a performed moderate seasonal pattern in general: lower in summer months and higher in colder months. Hussein et al.
314 (2019) also characterised the modal structure of the particle number size distribution for the same site. Four modes have
315 been detected by lognormal fitting, as known as DO-FIT algorithm and modal structure (Hussein et al., 2005; Hussein et
316 al., 2019), revealed that the mode number concentrations of the nucleation, Aitken, and coarse modes were lognormally
317 distributed around their geometric mean values: $0.022 \mu\text{m}$, $0.062 \mu\text{m}$, and $2.3 \mu\text{m}$ respectively. However, the accumulation
318 mode number concentration had two distinguished modes with particle diameter centred at $0.017 \mu\text{m}$ and $0.39 \mu\text{m}$. As
319 seen in Table 1, the total number concentration of all particle size ($1.70 \pm 1.26 \times 10^4 \text{ cm}^{-3}$) is mostly accounted by Aitken
320 mode (45–80%, average: $1.09 \pm 1.01 \times 10^4 \text{ cm}^{-3}$), followed by nucleation mode (10–50%, average: $0.48 \pm 0.32 \times 10^4 \text{ cm}^{-3}$).
321 Accumulation mode (0–15%, average: $0.13 \pm 0.08 \text{ cm}^{-3}$) comes third and only less than 0.5% of the total particle number
322 concentration contain coarse particles with an average of $2.13 \pm 2.80 \text{ cm}^{-3}$ (Figure 5b–e). Seasonal pattern of the total
323 number concentration resembles the Aitken composition: lower proportion in summer months and higher in colder
324 months. The ratio of nucleation mode performs in an opposite way. The seasonal variation of total number concentration
325 is due to the more suppressed boundary layer in winter (Teinilä et al., 2019) and the elevated wood combustion (Hellén
326 et al., 2017). The particle number of accumulation and coarse mode steadily stay at a low proportion line, which did not
327 account for the total number concentration. It is also noticed that dust episodes occurred with the concentrations that often
328 exceeded 2 cm^{-3} and the daily concentration in the course of these episodes can rise to 20 cm^{-3} . These episodes were often
329 found in spring from February to May and some episodes can last for up to one week.

330
331 Similar to many other urban environments, the diurnal pattern observed in this study reflects the combustion emissions
332 from traffic activity, which is more during the workdays (Hussein et al., 2019). The two peaks of the nucleation mode
333 and Aitken mode in the cold months are relevant for the morning and the afternoon traffic rush hours, which are similar
334 to those noticed in most cities in other countries. In warmer months, the diurnal cycles are not as distinct, but a sharp peak
335 of nucleation mode around noon is found, which is associated with the occurrence of new particle formation. These events
336 occurred very often in the summer as suggested by Hussein et al. (2020). The amplitude of diurnal cycles of coarse mode
337 is small while the patterns of accumulation are not clear (Figure 6).

338 3.3 Correlation analysis

339 Figure 7 demonstrated the interaction among the whole measured spectrum shows three range clusters based on their
340 correlation with the number concentration at other bin sizes: 0.01–0.205 μm , 0.205–0.875 μm and 0.875–10 μm . 0.01–
341 0.205 μm and 0.875–10 μm fall entirely within the size range detected by SMPS and OPS, respectively. The 5-min number
342 concentration of smaller size and bigger size bins have clear and strong correlation with the concentration of its
343 neighbouring size bin. However, particles of size 0.205–0.875 μm are located in the overlapping regions by the two
344 instruments; as a result, do not correlate well with other size bins. The correlation of 5-min particle size distribution with
345 meteorological parameters are generally low. Temperature appears to be the most correlated parameters for all bin sizes
346 among all the parameters we used in this study. Smaller size range have higher Pearson's correlation coefficient (R) than
347 larger size range for WD, WS and P.

348
349 The 5-min averaged data show similar correlation for the particle size distribution except for the smallest size bin. The
350 hourly and daily data have higher correlation with the other size bins which are also monitored by SMPS. The 5-min
351 averaged data show different correlation from the hourly and daily averaged data performed by Zaidan et al. (2020). The
352 correlations of 5-min size distribution with all meteorological variables are below 0.5 for all size range. However, for
353 hourly and daily averaged data, R is much higher in specific size bins. Hourly and daily temperature, in particular, show
354 increasing R with larger particle size for accumulation and coarse mode. Overall, the correlations increase with the longer
355 averaging windows. This might be due to the buffer period the meteorological conditions act on the dispersion of particles.
356 Based on this result, using data with finer temporal resolution might be considered to be less influential to the estimation
357 accuracy-of-modelling.

358 4 Model Evaluation of the proposed method

359 4.1 General evaluation

360 Figure 8 illustrates how well the models-of the three approaches of the proposed FFNN perform in term of R^2 and NRMSE.
361 **Approach 1 (Size distribution prediction-estimation based on meteorological parameters only, FFNN-met):** For
362 more than half out of the 23 size bins, 2 layers and 15 neurons is the best combination where the residuals are the lowest
363 (Table 2). Owing to Since the poor correlation with meteorological condition, we expect a low correlation of determination
364 even using the optimal configuration neural network ($R^2 = 0.22-0.58$). The R^2 looks-are low poor at the nucleation mode
365 ($0.01 < D_p < 0.03 \mu\text{m}$) of the whole size distribution around nucleation mode ($R^2 \sim 0.2$). The rest of the size bins have better
366 and more stable performance ($R^2 = 0.4-0.58$). This shows that the instrument might have a poor detection efficiency for
367 particles of smaller size. By using FFNN, The model-performance of FFNN method using 5-min data for all size bins
368 ($R^2 = 0.22-0.58$) is worse than using daily data ($R^2 = 0.77$) performed in Zaidan et al. (2020). Compared with hourly data
369 ($R^2 = 0.66$), the overall model-performance of the method using 5-min data is comparable ($R^2 = 0.67$).

370 **Approach 2 (SMutual size distribution prediction-estimation based on other particle sections only, FFNN-PSD):**
371 This approach works well with most combination of number of layers and neurons. They do did not show a clear difference
372 among the combinations we choose. There is no single combination which entirely outperform the others in all size bins.
373 We summed up the MAE for all size bins and decided to stick to 2 layers and 10 neurons with the overall lowest residuals
374 (Table 2). R^2 are all above 0.97 for all bin sizes, and NRMSE are is 0.01–0.25 for all bin sizes. The results are expected
375 because there are 22 inputs and one output. Relatively worse correlation at the edges of size bins ($0.01 < D_p < 0.02 \mu\text{m}$; $6 <$

Formatted: Subscript

Formatted: Subscript

376 $D_p < 10 \mu\text{m}$) is found because of the lack of nearby size bins which has high correlation with the corresponding size bin.
377 Another reason could be that the instrument has a higher detection limits for smaller particles (Liu et al., 2014). The
378 poorer performance for smaller size might be due to a coarser sizer resolution compared to other SMPS components
379 (Tritscher et al., 2013), so that NanoSMPS does not reflect the real enough size distribution in the atmosphere. Relatively
380 poor modelling-estimation performance at the middle size range ($0.15 < D_p < 0.5 \mu\text{m}$) in the whole measured spectrum is
381 because of the overlapping of instruments. This also ascertain the importance of creating a better algorithm when we
382 merge two or more size distribution by different instruments. In this study, the measuring techniques and the measuring
383 targets are different by the SMPS and OPS. The merging of the two measuring targets, the optical particle diameter and
384 the electrical mobility diameter, might create significant uncertainties (DeCarlo et al., 2004; Tritscher et al., 2015). The
385 estimation of certain bin size by other bin sizes can be thought of replacing negative values in the raw data by particle
386 sizers. While some instrument manufacturers create built-in algorithms to replace with artificial non-negative numbers,
387 most end-users simply remove the seemingly impossible negative values from the dataset. The perfect way to do it is to
388 have a parallel instrument that overlaps with that particle size range. However, in many cases, this is not possible as a
389 result of financial constraints. Therefore, we shall rely on the mutual relationship between the size sections in the aerosol
390 population. Negative values appear often at size bins with very low number concentration (usually in coarse mode).
391 Instead of eliminating them, this alternative could maintain the symmetry of the error distribution of the number
392 concentration (Viskari et al., 2012) and minimise the uncertainties caused.

393 **Approach 3 (~~SMutual-size distribution estimationprediction~~ based on meteorological parameters and other**
394 **particle sections):** The general results are similar as in PSD. However, the more input variables do not enable the
395 approachmodel to work better. At some bin size the R^2 are even slightly smaller than PSD solely. Since meteorological
396 data show low correlation with most portion of measured spectrum. In that approach, the addition of meteorological
397 parameters is not beneficial to the modelling-estimation process. Due to the lack of improvement in the methodmodel
398 development, we will only focus on the two methodsmodels: FFNN-met and FFNN-PSD from now on.

399
400 In order to highlight the performance of the FFNN methods in terms of accuracy and reliability, we compare the FFNN
401 methods with other simpler methods, the results as shown in Table 3 for R^2 and Table 4 for NRMSE. The R^2 of the
402 univariate methods UM and MD are close to 0 because their imputation are over-simplified and imply the replacement of
403 a missing value by a constant. The remaining univariate interpolation methods LinI, LogI, nNI and pNI showed good
404 results in general ($R^2 = 0.82-0.92$, $\text{NRMSE} = 0.57-0.88$), but failed to perform even fairly at some particle size bins. This
405 implies that these methods are not stable for the whole spectrum of the particle size distribution. The performance results
406 of the multivariate methods CM-met and CM-PSD are comparable to FFNN-met and FFNN-PSD, but both show weaker
407 performance in terms of R^2 and NRMSE no matter whether meteorological (CM-met: $R^2 = 0.52$, $\text{NRMSE} = 1.39$; FFNN-
408 met: $R^2 = 0.67$, $\text{NRMSE} = 1.13$) or particle size distribution data (CM-PSD: $R^2 = 0.99$, $\text{NRMSE} = 0.17$; FFNN-PSD: R^2
409 $= 1.00$, $\text{NRMSE} = 0.07$) is used as inputs. The pattern of performance of the multivariate methods is also similar to those
410 of FFNN, i.e., relatively poor performance at the edges of size bins ($0.01 < D_p < 0.02 \mu\text{m}$; $6 < D_p < 10 \mu\text{m}$) and the
411 overlapping region ($0.15 < D_p < 0.5 \mu\text{m}$). Although the multivariate method CM-PSD also rely on the mutual relationship
412 between the size sections in the aerosol population, this method is not as accurate as our proposed FFNN-PSD.

413
414 From the perspective of physics, particles in the nucleation mode ($0.01 < D_p < 0.03 \mu\text{m}$) are more sensitive to
415 transformation processes due to their volatility and rather unstable nature (Morawska et al., 2008). This leads to a

Formatted: Subscript

Formatted: Subscript

Formatted: Font color: Auto

Formatted: Subscript

416 relatively short lifetime in the atmosphere (Al-Dabbous et al., 2017), ~~therefore~~ hence, the relationships between the input
417 variables and the nucleation mode are not well established. Al-Dabbous et al. (2017) demonstrated that accumulation
418 mode particles ($0.1 < D_p < 0.3 \mu\text{m}$) have much longer lifetimes compared to smaller particles, causing them to be
419 transported for larger distances (Laakso et al., 2003); therefore, the mapping of the relationships between long-range
420 transported accumulation mode particles and covariates is supposed not to well understood. However, the relative
421 prediction ability in this study is not lower given that local meteorological variables were used as input variables. The
422 possible reason is that this mode falls exactly in the instrumental overlapping regions, which leads to a lower
423 ~~predictive~~ predictability. The locally-produced Aitken mode particles ($0.03 < D_p < 0.1 \mu\text{m}$) are less effectively removed
424 by transformation processes (e.g., evaporation and coagulation) from the atmosphere, compared with nucleation mode
425 ($0.01 < D_p < 0.03 \mu\text{m}$), allowing the ~~prediction model~~ estimation methods to better understand their relationships with the
426 input variables, which is in alignment with Al-Dabbous et al. (2017).

Formatted: Subscript

Formatted: Subscript

Formatted: Subscript

427 4.2 Temporal pattern

428 Figure 9 shows the diurnal discrepancies during workdays and weekends. Relative particle number concentration was
429 defined by the ~~estimated~~ modelled concentration with respect to the measured concentration. Values above 1 indicates
430 overestimation while values below 1 suggests underestimation. For approach 1 (FFNN-met), except for the overlapping
431 size bin, which are underestimated by more than 50% at all time range, the difference between ~~estimated~~ modelled and
432 measured hourly number concentration is within 50% during both workdays and weekends. Overestimation is found in
433 early morning before 3 a.m. during workdays for all size bins, especially for UFP. Following the overestimation, at about
434 6 a.m. in the morning, the ~~estimated~~ modelled number concentration appears to understate by up to 40%, especially at size
435 bins below $0.1 \mu\text{m}$. Along the day, the ~~modelling estimation~~ uncertainties are rather small until in the evening from 6
436 p.m. to 11 p.m. where ~~estimated~~ modelled UFP number concentration show moderate overestimation one more time. It
437 reveals that ~~the model with only meteorological parameters as inputs~~ FFNN-met fails to catch the diurnal pattern from 6
438 p.m. to 7 a.m. in particular for UFP. The pattern of the performance for weekends does not appear to be as distinctive as
439 on workdays. It shows the overestimation not only for UFP in early morning about 3 a.m., but also at the upper edge
440 larger than $5 \mu\text{m}$ from 3 a.m. to 4 p.m.. At 7 p.m. onwards until noon, an underestimation is found at all size bins. For
441 approach 2 (FFNN-PSD), except the overlapping size bin, which has a significant overestimation from 6 p.m. to 7 a.m.,
442 most show ~~trivial-negligible~~ 10% uncertainty during both workdays and weekends. The ~~model~~ performance over
443 weekends show relatively stronger uncertainties. The smallest bin at $0.01 \mu\text{m}$ is slightly understated for all hours of a day.
444 Other than these, ~~FFNN-PSD models with the full spectrum of size distribution as inputs~~ manages to catch fairly well the
445 diurnal pattern for all size bins.

446
447 Figure 10 further shows the monthly deviation in ~~estimation~~ modelling performance. For approach 1 (FFNN-met), higher
448 R^2 is found in November, February and April in the range of SMPS. Other than that, no observable variation in R^2 in
449 approach 1 (FFNN-met). For approach 2 (FFNN-PSD), except in January when all the rows were eliminated because of
450 the lack of wind information, performance in the other months is steady for most size range. At $0.21 \mu\text{m}$, the difference
451 in ~~estimation model~~ performance varies across different months. R^2 in winter months are 0.76, 0.36 and 0.61, in November,
452 December and February, respectively, while R^2 exceeds 0.9 in other months. This unexpectedly low R^2 only occurs in the
453 winter months at the overlapping size range. It can be speculated that the measurements by the two instruments differ in
454 a larger extent during winter. This might be attributed to sensor drift and a number of interference artefacts for particle

455 measurements associated with several factors, such as relative humidity, temperature and other gas-phase species, which
456 were demonstrated by several researchers (e.g. Lewis et al., 2016; Popoola et al., 2016). Another reason for the difference
457 in ~~estimationmodel~~ performance can be that the percentage of complete rows in these months are lower than the other
458 months. The drop in data points might impose an influence to the ~~estimationmodelling~~ performance. Especially in June,
459 at the few size bins close to the larger edge, R^2 ranges from 0.9 to 0.7. Besides that, some low R^2 can be also found in
460 individual month at both edges of size range, which does not appear to show any patterns.
461

462 In short, the ~~estimationprediction~~ ability for lower edge ($0.01 < D_p < 0.03 \mu\text{m}$) is found worse in both
463 ~~approachmodels~~. The ~~model~~ performance of the FFNN method in mid-range ($0.15 < D_p < 0.5 \mu\text{m}$) and upper edge
464 ($6 < D_p < 10 \mu\text{m}$) are relatively worse for ~~the approachmodel~~ with other fractionated size bins as input variables
465 according to the aforementioned statistical performance indicators. All statistical ~~estimationprediction~~ simulations
466 are based on the previous history of relationships between the inputs and outputs. As a result, the
467 ~~predictionestimation~~ simulations for different size ranges have significantly unique connections. The
468 ~~approachmodel~~ by meteorological parameters considers only 6 predictor variables so the accuracy is lower than
469 ~~the model by FFNN-PSD~~. It might not seem surprising that the deviations between the measured and estimated
470 size distribution were not substantial ($R^2 > 0.97$, $\text{NRMSE} < 0.25$) because ~~FFNN-PSDthe PSD model~~ takes 22 other
471 size bins as predictor variables. This, still, gives a clue that the proposed ~~FFNN methodmodel~~ can provide adequate
472 solutions to particle size distribution prognostic demands. ~~Furthermore, this FFNN method outperforms the other~~
473 ~~selected widely used methods in terms of its accuracy and reliability~~. The estimation of certain bin size by other
474 bin sizes can be thought of replacing 'negative' values in the raw data by particle sizers, including SMPS we used
475 in this paper. Instead of eliminating the negative values, they can be estimated by other size bins with a high
476 accuracy in order to keep the symmetry in data error distribution (Viskari et al., 2012).
477

478 5 Conclusion

479 This paper presents the evaluation of ~~imputation methods by means of~~ feed-forward neural network (FFNN) ~~models~~-for
480 estimating particle number concentration at various particulate size bins. Input predictors include a merged particle size
481 distribution, by a scanning mobility particle sizer (NanoSMPS) and an optical particle sizer (OPS), which covers size
482 range from 0.01 to 10, and meteorological parameters, including temperature (Temp), relative humidity (RH), wind
483 speed (WS), wind direction (WD) and ambient pressure (P). The measurements were collected in an urban background
484 region in Amman, the capital of Jordan in the period of 1st Aug 2016–31st July 2017. The total number concentration
485 ($1.70 \pm 1.26 \times 10^4 \text{ cm}^{-3}$) in the measurement period show moderate seasonal variability owing to the more suppressed
486 boundary layer (Teinilä et al., 2019) and the elevated wood combustion (Hellén et al., 2017) in wintertime. Similar to
487 many other urban environments, the diurnal pattern observed in this study reflects the traffic activity, which has a more
488 pronounced pattern during workdays (Hussein et al., 2019). The amount of coarse particles is ~~negligibletrivial~~ in terms of
489 number concentration but dust episodes were found often in spring during the measurement period.
490

491 We proposed three approaches with different input variables: (1) only meteorological parameters, (2) only number
492 concentration at the remaining size bins, and (3) both of the above. We performed optimisation to obtain the optimal
493 configuration of the FFNN ~~methodsmodels~~, which are two layers with 10–15 neurons, balancing the accuracy and the
494 computing resources. The 5-min averaged meteorological parameters give varying number concentration estimation for
495 various size bins ($R^2 = 0.22\text{--}0.58$), which is outperformed by hourly and daily averaged data ($R^2 = 0.66\text{--}0.77$), as
496 demonstrated by Zaidan et al. (2020). The ~~methodsmodels~~ using the number concentration at the remaining size bins,

Formatted: Subscript

Formatted: Subscript

Formatted: Subscript

Formatted: Superscript

497 both with or without meteorological data, show expected perfect performance ($R^2 > 0.97$). We also compare the FFNN
498 methods with other commonly used methods and the results highlight the high accuracy and reliability of methods by
499 means of neural networks.

500
501 Relatively poor ~~model~~-performance of the proposed FFNN methods is found in three regions. At the lower edge ($0.01 <$
502 $D_p < 0.02 \mu\text{m}$) and the upper edge ($6 < D_p < 10 \mu\text{m}$), the number of neighbouring size bins is limited and also the detection
503 efficiency by the corresponding instruments is lower compared to the other size bins. Another noticeable region ($0.15 <$
504 $D_p < 0.5 \mu\text{m}$) is the overlapping section measured by the two particle sizers and the reason is because of the deficiency of
505 merging algorithm. For all the above approaches, the poorer performance for smaller particles in the nucleation mode
506 could be due to the fact that it is more effectively removed from the atmosphere compared to other modes (Al-Dabbous
507 et al., 2017). An observable overestimation is also found in early morning for ultrafine particles followed by a distinct
508 underestimation before midday. A larger derivation between the measured and the estimated number concentration is
509 found in the winter, which might be caused by sensor drift and interference artefacts (e.g. Lewis et al., 2016; Popoola et
510 al., 2016). Despite the high number of input predictors, the good ~~emodel~~stimulation performance provides an alternative
511 method to fill up the negative values in size distribution raw dataset, which often exist due to ~~mis~~
512 ~~configured~~misconfiguration problems. Instead of removing the factually impossible data point, this way of replacing
513 negative numbers can maintain a symmetric distribution of errors (Viskari et al., 2012) and minimise the uncertainties
514 caused.

Formatted: Subscript

Formatted: Subscript

Formatted: Subscript

515 **Code/Data availability**

516 The code and data is available upon request.

517 **Author contribution**

518 TH and MZ designed the experiments and TH carried them out. PLF and OS developed the ~~model~~-code of the proposed
519 FFNN methods. PLF prepared the manuscript with contributions from all co-authors.

520 **Competing interests**

521 The authors declare that they have no conflict of interest.

522

523 **Financial support**

524 The work is supported by MegaSense program, the City of Helsinki Innovation Fund, Business Finland, the European
525 Union through the Urban Innovative Action Healthy Outdoor Premises for Everyone (HOPE, project No. UIA03-240).
526 This research is also funded by the Scientific Research Support Fund (SRF, Project Number BAS-1-2-2015) at the
527 Jordanian Ministry of Higher Education and the Deanship of Academic Research (DAR, Project Number 1516) at the
528 University of Jordan. This research is part of a close collaboration between the University of Jordan and the Institute for
529 Atmospheric and Earth System Research (INAR/Physics, University of Helsinki) via ERC advanced Grant No. 742206.

Formatted: Heading 1

530 the European Union's Horizon 2020 research and innovation program under Grant Agreement No. 654109, the Academy
531 of Finland Flagship funding (Project No. 337549), ERA-PLANET (www.era-planet.eu), trans-national project SMURBS
532 (www.smurbs.eu, Grant Agreement No. 689443) funded under the EU Horizon 2020 Framework Programme, and
533 Academy of Finland via the Center of Excellence in Atmospheric sciences and NanoBioMass (Project Number 1307537).

Formatted: Not Highlight

Formatted: Not Highlight

534 References

- 535 Ahmed, R., Robinson, R., and Mortimer, K.: The epidemiology of noncommunicable respiratory disease in sub-Saharan
536 Africa, the Middle East, and North Africa, *Malawi Med J*, 29, 203-211, <https://doi.org/10.4314/mmj.v29i2.24>, 2017.
- 537 Al-Dabbous, A. N., Kumar, P., and Khan, A. R.: Prediction of airborne nanoparticles at roadside location using a feed-
538 forward artificial neural network, *Atmos Pollut Res*, 8, 446-454, <https://doi.org/10.1016/j.apr.2016.11.004>, 2017.
- 539 Arhami, M., Shahne, M. Z., Hosseini, V., Haghighat, N. R., Lai, A. M., and Schauer, J. J.: Seasonal trends in the
540 composition and sources of PM_{2.5} and carbonaceous aerosol in Tehran, Iran, *Environ Pollut*, 239, 69-81,
541 <https://doi.org/10.1016/j.envpol.2018.03.111>, 2018.
- 542 Borgie, M., Ledoux, F., Dagher, Z., Verdin, A., Cazier, F., Courcot, L., Shirali, P., Greige-Gerges, H., and Courcot, D.:
543 Chemical characteristics of PM_{2.5}-0.3 and PM_{0.3} and consequence of a dust storm episode at an urban site in Lebanon,
544 *Atmos Res*, 180, 274-286, <https://doi.org/10.1016/j.atmosres.2016.06.001>, 2016.
- 545 Cabaneros, S. M., Calautit, J. K., and Hughes, B. R.: A review of artificial neural network models for ambient air pollution
546 prediction, *Environ Modell Softw*, 119, 285-304, <https://doi.org/10.1016/j.envsoft.2019.06.014>, 2019.
- 547 Cai, R., Yang, D., Ahonen, L. R., Shi, L., Korhonen, F., Ma, Y., Hao, J., Petäjä, T., Zheng, J., Kangasluoma, J., and Jiang,
548 J.: Data inversion methods to determine sub-3 nm aerosol size distributions using the particle size magnifier, *Atmos Meas*
549 *Tech*, 11, 4477-4491, <https://doi.org/10.5194/amt-11-4477-2018>, 2018.
- 550 Chaloulakou, A., Grivas, G., and Spyrellis, N.: Neural network and multiple regression models for PM₁₀ prediction in
551 Athens: a comparative assessment, *J Air Waste Manag Assoc*, 53, 1183-1190,
552 <https://doi.org/10.1080/10473289.2003.10466276>, 2003.
- 553 DeCarlo, P. F., Slowik, J. G., Worsnop, D. R., Davidovits, P., and Jimenez, J. L.: Particle morphology and density
554 characterization by combined mobility and aerodynamic diameter measurements. Part 1: Theory, *Aerosol Sci Tech*, 38,
555 1185-1205, <https://doi.org/10.1080/027868290903907>, 2004.
- 556 Enting, I., and Newsam, G.: Atmospheric constituent inversion problems: Implications for baseline monitoring, *J Atmos*
557 *Chem*, 11, 69-87, <https://doi.org/10.1007/BF00053668>, 1990.
- 558 Fonseca, A. S., Viana, M., Perez, N., Alastuey, A., Querol, X., Kaminski, H., Todea, A. M., Monz, C., and Asbach, C.:
559 Intercomparison of a portable and two stationary mobility particle sizers for nanoscale aerosol measurements, *Aerosol*
560 *Sci Tech*, 50, 653-668, <https://doi.org/10.1080/02786826.2016.1174329>, 2016.
- 561 Freeman, B. S., Taylor, G., Gharabaghi, B., and Thé, J.: Forecasting air quality time series using deep learning, *J Air*
562 *Waste Manag Assoc*, 68, 866-886, <https://doi.org/10.1080/10962247.2018.1459956>, 2018.
- 563 Gherboudj, I., Beegum, S. N., and Ghedira, H.: Identifying natural dust source regions over the Middle-East and North-
564 Africa: Estimation of dust emission potential, *Earth-Sci Rev*, 165, 342-355,
565 <https://doi.org/10.1016/j.earscirev.2016.12.010>, 2017.
- 566 Goudarzi, G., Shirmardi, M., Naimabadi, A., Ghadiri, A., and Sajedifar, J.: Chemical and organic characteristics of PM_{2.5}
567 particles and their in-vitro cytotoxic effects on lung cells: The Middle East dust storms in Ahvaz, Iran, *Sci Total Environ*,
568 655, 434-445, <https://doi.org/10.1016/j.scitotenv.2018.11.153>, 2019.
- 569 Gupta, R., and Xie, H.: Nanoparticles in Daily Life: Applications, Toxicity and Regulations, *J Environ Pathol Toxicol*
570 *Oncol*, 37, 209-230, <https://doi.org/10.1615/JEnvironPatholToxicolOncol.2018026009>, 2018.
- 571 Hakala, S., Alghamdi, M. A., Paasonen, P., Vakkari, V., Khoder, M. I., Neitola, K., Dada, L., Abdelmaksoud, A. S., Al-
572 Jeelani, H., Shabbaj, I. I., Almeahadi, F. M., Sundström, A. M., Lihavainen, H., Kerminen, V. M., Kontkanen, J.,
573 Kulmala, M., Hussein, T., and Hyvärinen, A. P.: New particle formation, growth and apparent shrinkage at a rural
574 background site in western Saudi Arabia, *Atmos Chem Phys*, 19, 10537-10555, <https://doi.org/10.5194/acp-19-10537-2019>, 2019.
- 575 Hellén, H., Kangas, L., Kousa, A., Vestenius, M., Teinilä, K., Karppinen, A., Kukkonen, J., and Niemi, J. V.: Evaluation
576 of the impact of wood combustion on benzo[a]pyrene (BaP) concentrations; ambient measurements and dispersion
577 modeling in Helsinki, Finland, *Atmos Chem Phys*, 17, 3475-3487, <https://doi.org/10.5194/acp-17-3475-2017>, 2017.
- 578 Hussein, T., Dal Maso, M., Petäjä, T., Koponen, I. K., Paatero, P., Aalto, P. P., Hämeri, K., and Kulmala, M.: Evaluation
579 of an automatic algorithm for fitting the particle number size distributions, *Boreal Environ Res*, 10, 337-355, 2005.
- 580 Hussein, T., Dada, L., Hakala, S., Petäjä, T., and Kulmala, M.: Urban Aerosol Particle Size Characterization in Eastern
581 Mediterranean Conditions, *Atmosphere*, 10, 10.3390/atmos10110710, 2019.
- 582 Hussein, T., Atashi, N., Sogacheva, L., Hakala, S., Dada, L., Petäjä, T., and Kulmala, M.: Characterization of Urban New
583 Particle Formation in Amman—Jordan, *Atmosphere*, 11, 10.3390/atmos11010079, 2020.
- 584

585 Junger, W., and Ponce De Leon, A.: Imputation of missing data in time series for air pollutants, *Atmos Environ*, 102, 96-
586 104, <https://doi.org/10.1016/j.atmosenv.2014.11.049>, 2015.

587 Kandlikar, M., and Ramachandran, G.: Inverse methods for analysing aerosol spectrometer measurements: a critical
588 review, *J Aerosol Sci*, 30, 413-437, [https://doi.org/10.1016/S0021-8502\(98\)00066-4](https://doi.org/10.1016/S0021-8502(98)00066-4), 1999.

589 Kannosto, J., Virtanen, A., Lemmetty, M., Mäkelä, J. M., Keskinen, J., Junninen, H., Hussein, T., Aalto, P., and Kulmala,
590 M.: Mode resolved density of atmospheric aerosol particles, *Atmos Chem Phys*, 8, 5327-5337,
591 <https://doi.org/10.5194/acp-8-5327-2008>, 2008.

592 Kerminen, V. M., Paramonov, M., Anttila, T., Riipinen, I., Fountoukis, C., Korhonen, H., Asmi, E., Laakso, L.,
593 Lihavainen, H., Swietlicki, E., Svenningsson, B., Asmi, A., Pandis, S. N., Kulmala, M., and Petaja, T.: Cloud
594 condensation nuclei production associated with atmospheric nucleation: a synthesis based on existing literature and new
595 results, *Atmos Chem Phys*, 12, 12037-12059, <https://doi.org/10.5194/acp-12-12037-2012>, 2012.

596 Kerminen, V. M., Chen, X. M., Vakkari, V., Petaja, T., Kulmala, M., and Bianchi, F.: Atmospheric new particle formation
597 and growth: review of field observations, *Environ Res Lett*, 13, <https://doi.org/10.1088/1748-9326/aadf3c>, 2018.

598 Kok, J. F., Ridley, D. A., Zhou, Q., Miller, R. L., Zhao, C., Heald, C. L., Ward, D. S., Albani, S., and Hausteine, K.:
599 Smaller desert dust cooling effect estimated from analysis of dust size and abundance, *Nat Geosci*, 10, 274-278,
600 <https://doi.org/10.1038/Ngeo2912>, 2017.

601 Kreyling, W. G., Semmler, M., and Moller, W.: Dosimetry and toxicology of ultrafine particles, *J Aerosol Med*, 17, 140-
602 152, <https://doi.org/10.1089/0894268041457147>, 2004.

603 Kulkarni, P., Baron, P. A., and Willeke, K.: Aerosol measurement: principles, techniques, and applications, John Wiley
604 & Sons, 2011.

605 Kulmala, M., Vehkamäki, H., Petaja, T., Dal Maso, M., Lauri, A., Kerminen, V. M., Birmili, W., and McMurry, P. H.:
606 Formation and growth rates of ultrafine atmospheric particles: a review of observations, *J Aerosol Sci*, 35, 143-176,
607 <https://doi.org/10.1016/j.jaerosci.2003.10.003>, 2004.

608 Laakso, L., Hussein, T., Aarnio, P., Komppula, M., Hiltunen, V., Viisanen, Y., and Kulmala, M.: Diurnal and annual
609 characteristics of particle mass and number concentrations in urban, rural and Arctic environments in Finland, *Atmos
610 Environ*, 37, 2629-2641, [https://doi.org/10.1016/S1352-2310\(03\)00206-1](https://doi.org/10.1016/S1352-2310(03)00206-1), 2003.

611 Lehtipalo, K., Leppä, J., Kontkanen, J., Kangasluoma, J., Franchin, A., Wimmer, D., Schobesberger, S., Junninen, H.,
612 Petaja, T., Sipilä, M., Mikkilä, J., Vanhanen, J., Worsnop, D. R., and Kulmala, M.: Methods for determining particle size
613 distribution and growth rates between 1 and 3 nm using the Particle Size Magnifier, *Boreal Environ Res*, 2014.

614 Lelieveld, J., Evans, J. S., Fnais, M., Giannadaki, D., and Pozzer, A.: The contribution of outdoor air pollution sources to
615 premature mortality on a global scale, *Nature*, 525, 367-371, <https://doi.org/10.1038/nature15371>, 2015.

616 Lewis, A. C., Lee, J. D., Edwards, P. M., Shaw, M. D., Evans, M. J., Moller, S. J., Smith, K. R., Buckley, J. W., Ellis,
617 M., Gillot, S. R., and White, A.: Evaluating the performance of low cost chemical sensors for air pollution research,
618 *Faraday Discuss*, 189, 85-103, <https://doi.org/10.1039/c5fd000201j>, 2016.

619 Liu, Z. R., Hu, B., Liu, Q., Sun, Y., and Wang, Y. S.: Source apportionment of urban fine particle number concentration
620 during summertime in Beijing, *Atmos Environ*, 96, 359-369, <https://doi.org/10.1016/j.atmosenv.2014.06.055>, 2014.

621 Londahl, J., Moller, W., Pagels, J. H., Kreyling, W. G., Swietlicki, E., and Schmid, O.: Measurement techniques for
622 respiratory tract deposition of airborne nanoparticles: a critical review, *J Aerosol Med Pulm Drug Deliv*, 27, 229-254,
623 <https://doi.org/10.1089/jamp.2013.1044>, 2014.

624 Maleki, H., Sorooshian, A., Goudarzi, G., Baboli, Z., Birgani, Y. T., and Rahmati, M.: Air pollution prediction by using
625 an artificial neural network model, *Clean Technol Environ Policy*, 21, 1341-1352, [https://doi.org/10.1007/s10098-019-
626 01709-w](https://doi.org/10.1007/s10098-019-

626 01709-w), 2019.

627 Markowski, G. R.: Improving Twomey's algorithm for inversion of aerosol measurement data, *Aerosol Sci Tech*, 7, 127-
628 141, <https://doi.org/10.1080/02786828708959153>, 1987.

629 Morawska, L., Ristovski, Z., Jayaratne, E. R., Keogh, D. U., and Ling, X.: Ambient nano and ultrafine particles from
630 motor vehicle emissions: Characteristics, ambient processing and implications on human exposure, *Atmos Environ*, 42,
631 8113-8138, <https://doi.org/10.1016/j.atmosenv.2008.07.050>, 2008.

632 Ohlwein, S., Kappeler, R., Joss, M. K., Kunzli, N., and Hoffmann, B.: Health effects of ultrafine particles: a systematic
633 literature review update of epidemiological evidence, *Int J Public Health*, 64, 547-559, [https://doi.org/10.1007/s00038-
634 019-01202-7](https://doi.org/10.1007/s00038-

634 019-01202-7), 2019.

635 Popoola, O. A. M., Stewart, G. B., Mead, M. I., and Jones, R. L.: Development of a baseline-temperature correction
636 methodology for electrochemical sensors and its implications for long-term stability, *Atmos Environ*, 147, 330-343,
637 <https://doi.org/10.1016/j.atmosenv.2016.10.024>, 2016.

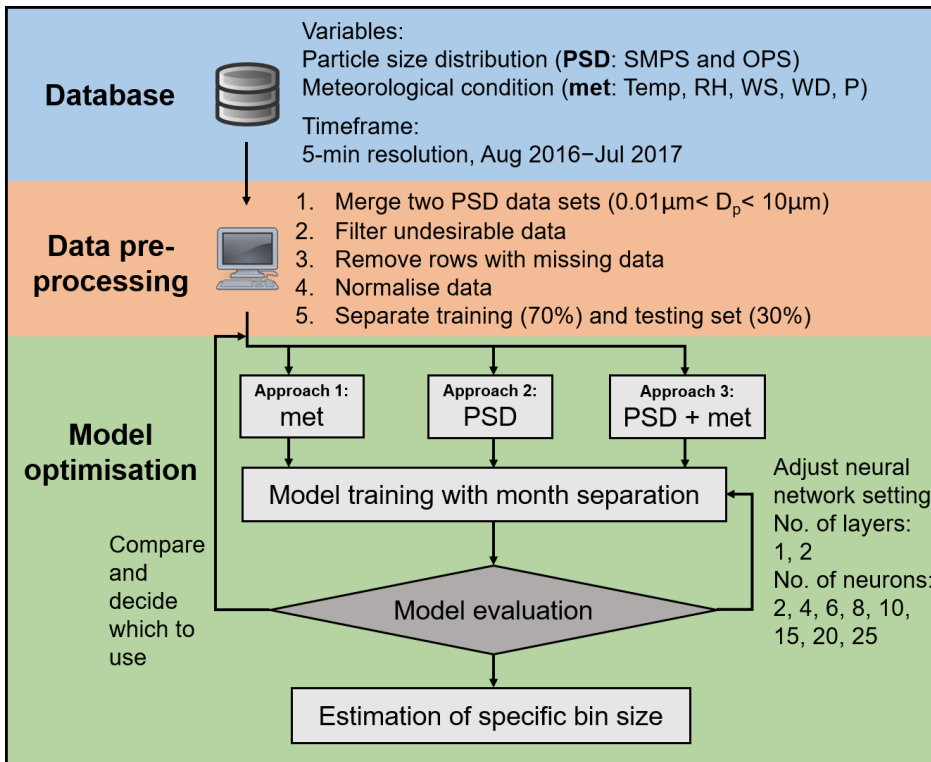
638 Rönkkö, T., Kuuluvainen, H., Karjalainen, P., Keskinen, J., Hillamo, R., Niemi, J. V., Pirjola, L., Timonen, H. J.,
639 Saarikoski, S., Saukko, E., Jarvinen, A., Silvennoinen, H., Rostedt, A., Olin, M., Yli-Ojanpera, J., Nousiainen, P., Kousa,
640 A., and Dal Maso, M.: Traffic is a major source of atmospheric nanocluster aerosol, *P Natl Acad Sci USA*, 114, 7549-
641 7554, <https://doi.org/10.1073/pnas.1700830114>, 2017.

642 Spinazzè, A., Fantì, G., Borghi, F., Del Buono, L., Campagnolo, D., Rovelli, S., Cattaneo, A., and Cavallo, D. M.: Field
643 comparison of instruments for exposure assessment of airborne ultrafine particles and particulate matter, *Atmos Environ*,
644 154, 274-284, <https://doi.org/10.1016/j.atmosenv.2017.01.054>, 2017.

645 Stolzenburg, M. R., and McMurry, P. H.: Method to assess performance of scanning mobility particle sizer (SMPS)
646 instruments and software, *Aerosol Sci Tech*, 52, 609–613, <https://doi.org/10.1080/02786826.2018.1455962>, 2018.
647 Teinilä, K., Aurela, M., Niemi, J. V., Kousa, A., Petäjä, T., Järvi, L., Hillamo, R., Kangas, L., Saarikoski, S., and Timonen,
648 H.: Concentration variation of gaseous and particulate pollutants in the Helsinki city centre — observations from a two-
649 year campaign from 2013–2015, *Boreal Environ Res*, 24, 115–136, 2019.
650 Tritscher, T., Beeston, M., Zerrath, A. F., Elzey, S., Krinke, T. J., Filimundi, E., and Bischof, O. F.: NanoScan SMPS -
651 A Novel, Portable Nanoparticle Sizing and Counting Instrument, *J Phys: Conf Ser*, 429, 012061,
652 <https://doi.org/10.1088/1742-6596/429/1/012061>, 2013.
653 Tritscher, T., Koched, A., Han, H. S., Filimundi, E., Johnson, T., Elzey, S., Avenido, A., Kykal, C., and Bischof, O. F.:
654 Multi-Instrument Manager Tool for Data Acquisition and Merging of Optical and Electrical Mobility Size Distributions,
655 *J Phys: Conf Ser*, 617, 012013, <https://doi.org/10.1088/1742-6596/617/1/012013>, 2015.
656 Viskari, T., Asmi, E., Kolmonen, P., Vuollekoski, H., Petaja, T., and Jarvinen, H.: Estimation of aerosol particle number
657 distributions with Kalman Filtering - Part 1: Theory, general aspects and statistical validity, *Atmos Chem Phys*, 12, 11767-
658 11779, <https://doi.org/10.5194/acp-12-11767-2012>, 2012.
659 Wiedensohler, A., Birmili, W., Nowak, A., Sonntag, A., Weinhold, K., Merkel, M., Wehner, B., Tuch, T., Pfeifer, S.,
660 Fiebig, M., Fjåraa, A. M., Asmi, E., Sellegri, K., Depuy, R., Venzac, H., Villani, P., Laj, P., Aalto, P., Ogren, J. A.,
661 Swietlicki, E., Williams, P., Roldin, P., Quincey, P., Hüglin, C., Fierz-Schmidhauser, R., Gysel, M., Weingartner, E.,
662 Riccobono, F., Santos, S., Gruning, C., Faloon, K., Beddows, D., Harrison, R., Monahan, C., Jennings, S. G., O'Dowd,
663 C. D., Marinoni, A., Horn, H. G., Keck, L., Jiang, J., Scheckman, J., McMurry, P. H., Deng, Z., Zhao, C. S., Moerman,
664 M., Henzing, B., de Leeuw, G., Löschau, G., and Bastian, S.: Mobility particle size spectrometers: harmonization of
665 technical standards and data structure to facilitate high quality long-term observations of atmospheric particle number
666 size distributions, *Atmos Meas Tech*, 5, 657–685, <https://doi.org/10.5194/amt-5-657-2012>, 2012.
667 Population growth (annual %): <https://data.worldbank.org/indicator/SP.POP.GROW>, access: 06-10, 2019.
668 World Health Organisation: World health statistics 2019: Monitoring health for the SDGs, sustainable development goals,
669 World Health Organisation, <https://apps.who.int/iris/handle/10665/324835>, 2019.
670 Xing, Y. F., Xu, Y. H., Shi, M. H., and Lian, Y. X.: The impact of PM2.5 on the human respiratory system, *J Thorac Dis*,
671 8, E69-74, <https://doi.org/10.3978/j.issn.2072-1439.2016.01.19>, 2016.
672 Zaidan, M. A., Canova, F. F., Laurson, L., and Foster, A. S.: Mixture of Clustered Bayesian Neural Networks for
673 Modeling Friction Processes at the Nanoscale, *J Chem Theory Comput*, 13, 3-8, <https://doi.org/10.1021/acs.jctc.6b00830>,
674 2017.
675 Zaidan, M. A., Surakhi, O., Fung, P. L., and Hussein, T.: Sensitivity Analysis for Predicting Sub-Micron Aerosol
676 Concentrations Based on Meteorological Parameters, *Sensors (Basel)*, 20, <https://doi.org/10.3390/s20102876>, 2020.
677 Zhou, Y., Dada, L., Liu, Y., Fu, Y., Kangasluoma, J., Chan, T., Yan, C., Chu, B., Daellenbach, K. R., Bianchi, F.,
678 Kokkonen, T. V., Liu, Y., Kujansuu, J., Kerminen, V.-M., Petäjä, T., Wang, L., Jiang, J., and Kulmala, M.: Variation of
679 size-segregated particle number concentrations in wintertime Beijing, *Atmos Chem Phys*, 20, 1201-1216,
680 <https://doi.org/10.5194/acp-20-1201-2020>, 2020.

681

Formatted: German (Germany)



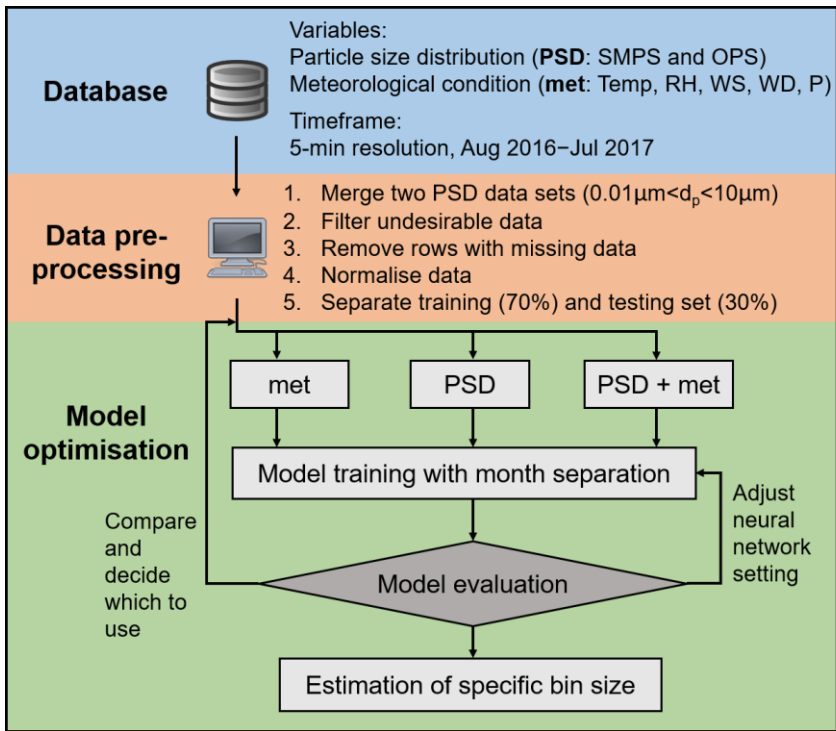


Figure 1. The block diagram describing the methodology of the proposed FFNN method-model.

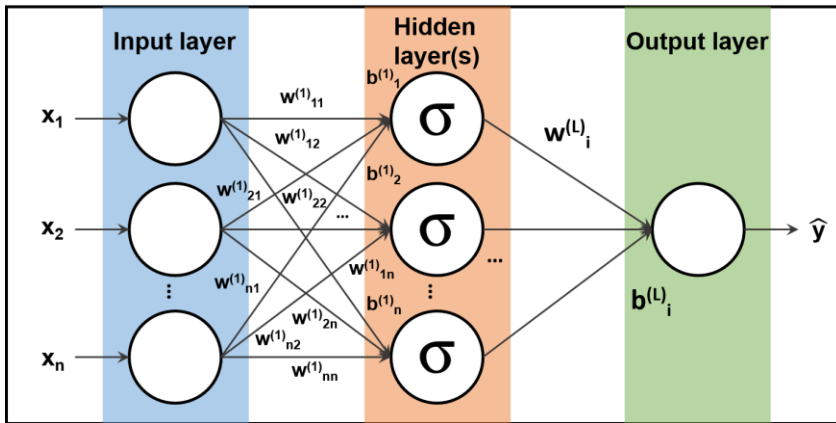


Figure 2. Schematic diagram of a neural network with one hidden layer of sigmoid activation function.

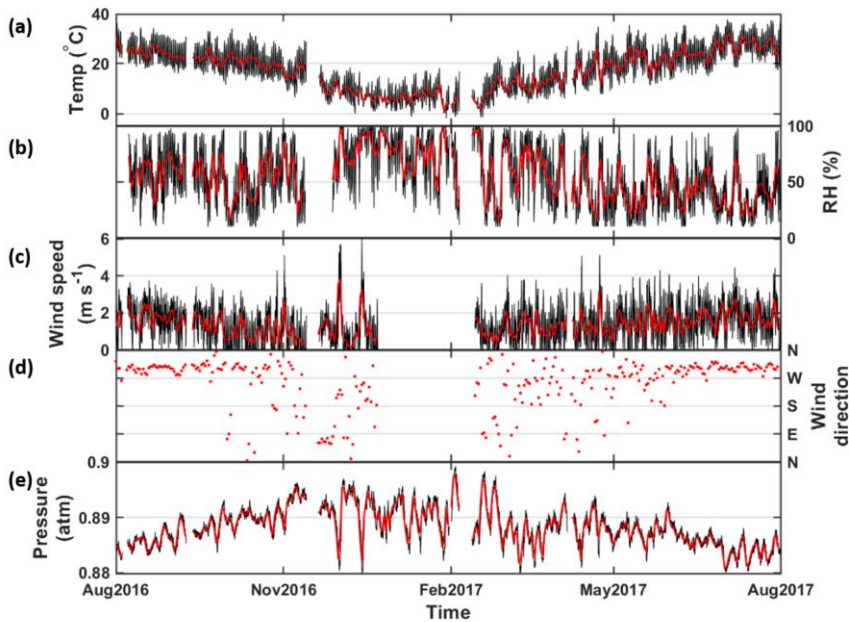


Figure 3. Timeseries of meteorological conditions during the measurement period Aug 2016–Jul 2017. (a–e) denotes temperature, relative humidity, wind speed, wind direction and air pressure, respectively. Black and red represent hourly and daily averaged data, respectively.

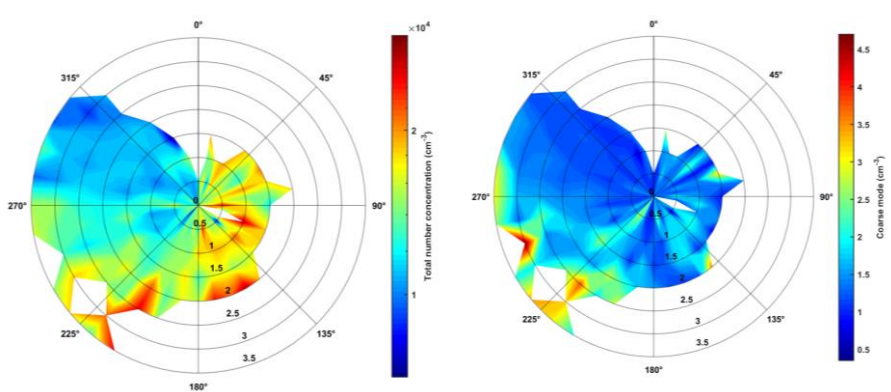


Figure 4. Windrose diagram of total particle number concentration at different direction (in theta axis) and different wind speed (in radial axis). Wind direction and wind speed data are grouped in every 10° and 0.5 m s^{-1} . Warmer color represent higher total particle number concentration. (a) total number concentration, log scale; (b) coarse mode, linear scale. Note the color scales are different.

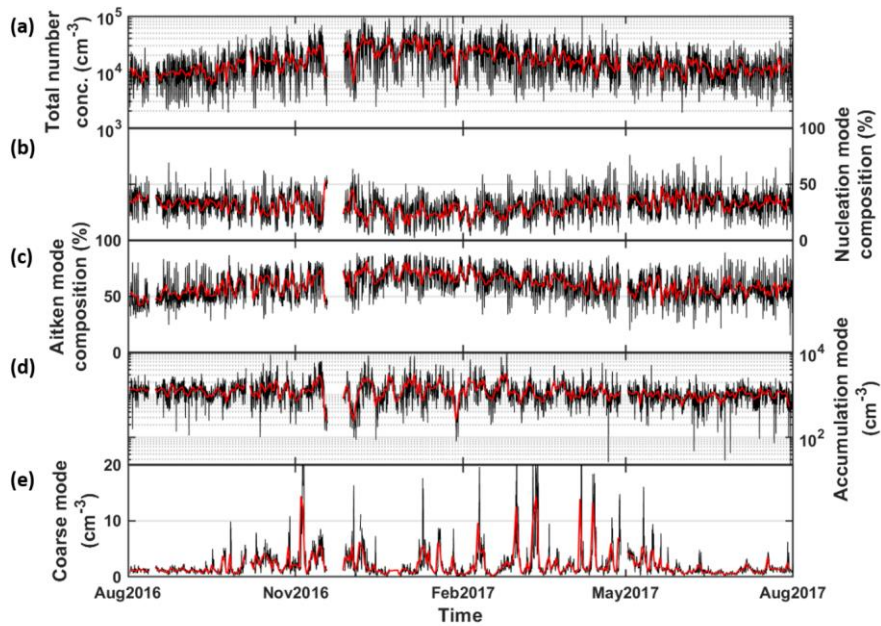


Figure 5. Timeseries of total particle number concentration (in cm^{-3}) of $0.01\text{--}10\mu\text{m}$ in (a). (b–c) indicate the contribution in percentage of nucleation mode and Aitken mode, respectively. (d–e) show the number concentration in accumulation mode and coarse mode, respectively. Black and red represent hourly and daily averaged data, respectively.

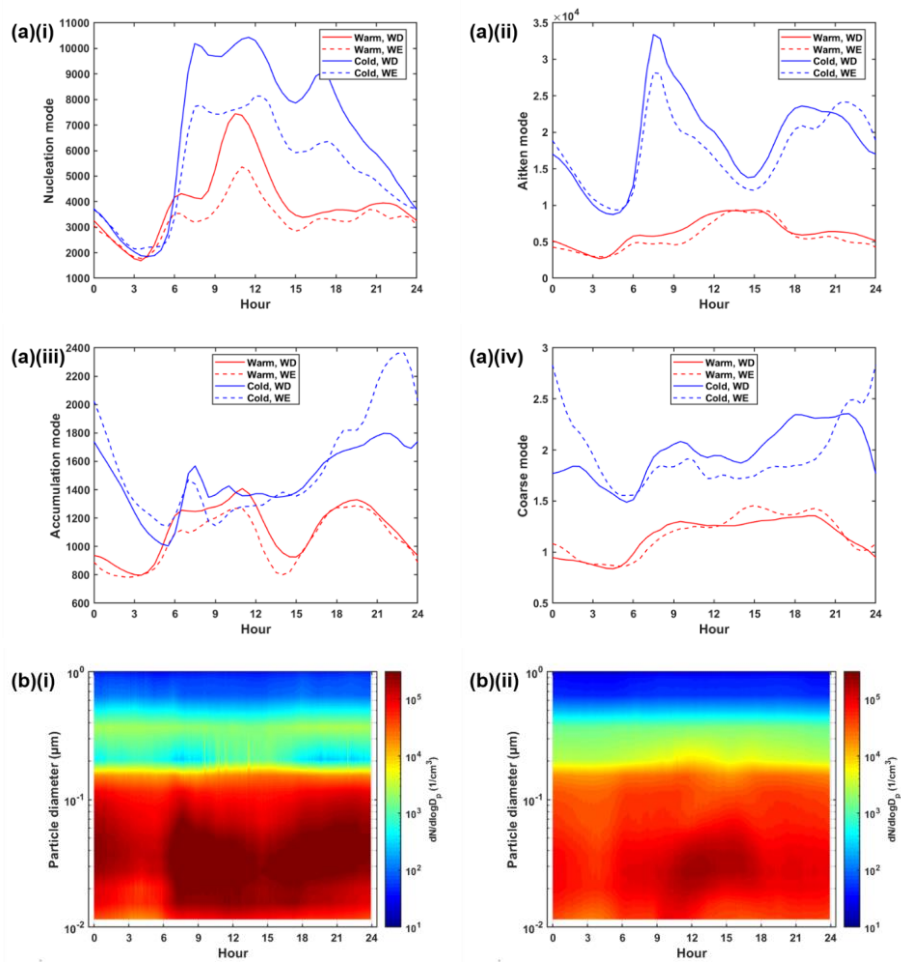


Figure 6. (a) Diurnal cycle of the (i) nucleation mode, (ii) Aitken mode, (iii) accumulation mode and (iv) coarse mode in warm (red) and cold months (blue) during workdays (solid) and weekends (dashed). (b) Particle size distribution in (i) cold and (ii) warm months, coloured by particle number concentration (cm^{-3}). Cold and warm months refer to December–February and June–August, respectively.

Formatted: Line spacing: single

Formatted: English (United States)

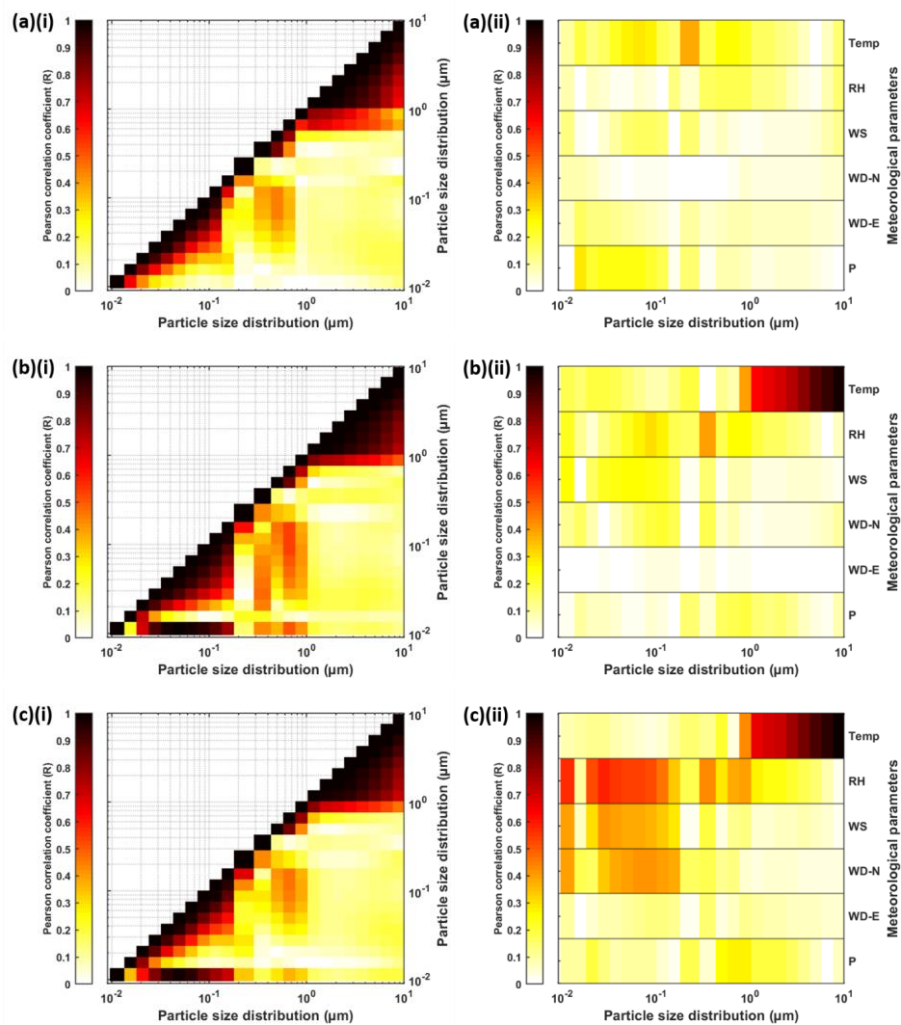
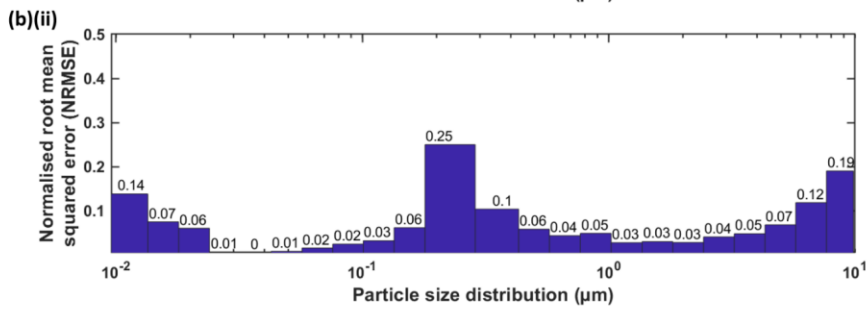
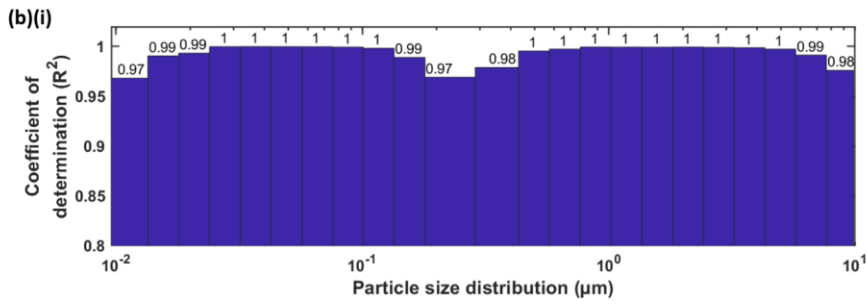
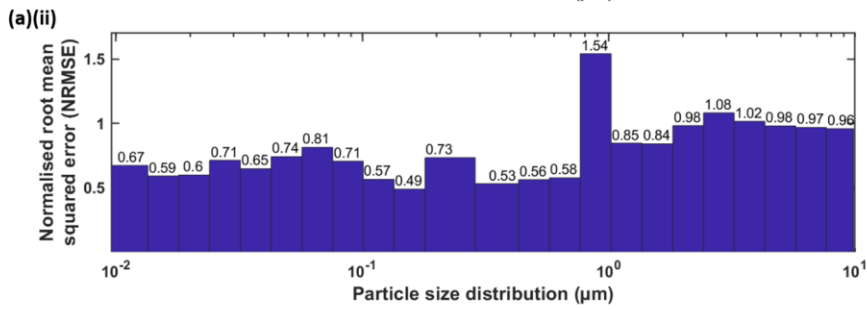
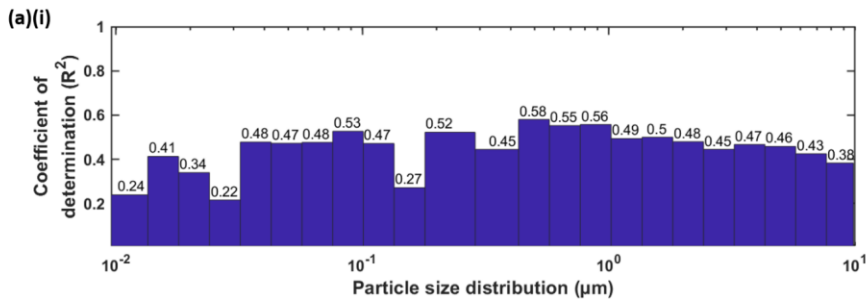


Figure 7. Matrix plots showing the Pearson correlation coefficient (R) of particle size distribution of (a) 5-min, (b) hourly, (c) daily averaging with (i) particle size distribution itself and (ii) meteorological parameters. Darker colour represents a higher correlation.



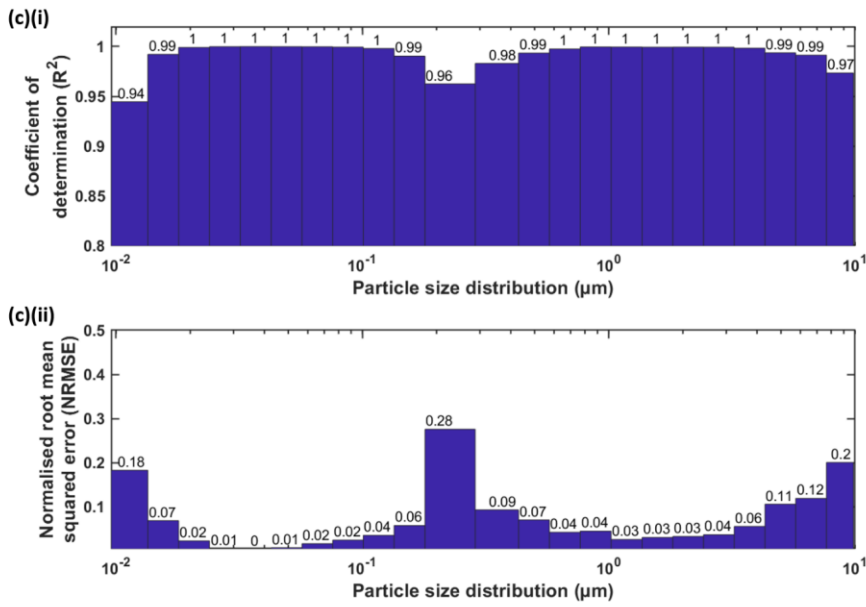


Figure 8. Bar chart showing the model-evaluation of FFNN model approach with (a) only meteorological parameters (Approach 1, FFNN-met), (b) particle size distribution itself (Approach 2, FFNN-PSD), (c) both particle size distribution and meteorological parameters (Approach 3) as inputs. The model-evaluation metrics for the proposed method include (i) coefficient of determination (R²) and (ii) normalised root mean squared error (NRMSE).

Formatted: Line spacing: single

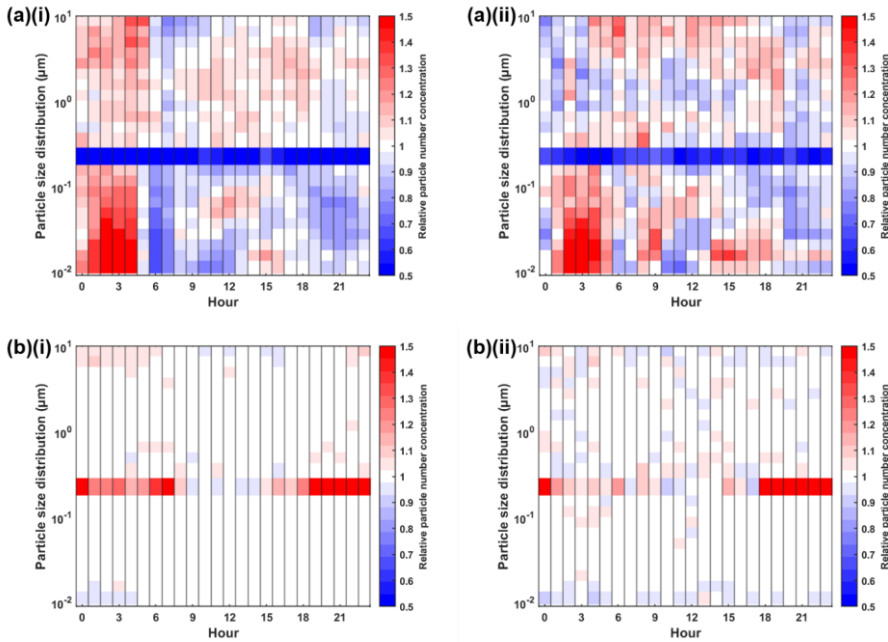


Figure 9. Heatmap showing the hourly median relative particle number concentration of the **models-approach** with (a) meteorological parameters (**Approach 1, FFNN-met**) and (b) particle size distribution- (**Approach 2, FFNN-PSD**) as inputs across different hours of a day (i) in workdays and (ii) in weekends. The relative particle number concentration is defined as **estimated** concentration with respect to measured concentration. Red colour show overestimation while blue show underestimation.

Formatted: Font: 10 pt, Not Italic, Font color: Auto

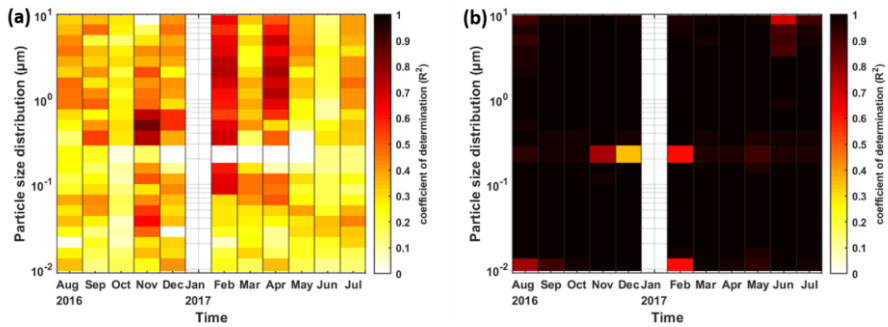


Figure 10. Heatmap showing the coefficient of determination (R^2) of the **approachmodels** with (a) meteorological parameters (**Approach 1, FFNN-met**) and (b) particle size distribution (**Approach 2, FFNN-PSD**) as inputs for different months at different size bins. Darker colour represents a higher R^2 .

683 Table 1. Table showing the descriptive statistics (in cm^{-3}) of total number concentration, nucleation mode, Aitken mode,
 684 accumulation mode and coarse mode. The statistical values include mean, standard deviation, and percentile (10%, 25%,
 685 50%, 75% and 90%).

	Mean	std	10%	25%	50%	75%	90%
Total ($\times 10^4$)	1.70	1.26	0.57	0.85	1.35	2.16	3.31
Nucleation ($\times 10^4$)	0.48	0.32	0.16	0.26	0.41	0.63	0.90
Aitken ($\times 10^4$)	1.09	1.01	0.29	0.45	0.77	1.37	2.35
Accumulation ($\times 10^4$)	0.13	0.08	0.05	0.08	0.11	0.15	0.21
Coarse	2.13	2.80	0.55	0.84	1.29	2.33	4.3

686

687 Table 2. Table showing the best configuration in the form of (the number of layers; the number of neurons) for the
 688 approach model by meteorological parameters (FFNN-met) and the number concentration at the other size bins (FFNN-
 689 PSD as inputs). Mean absolute error (MAE, in cm^{-3}), coefficient of determination (R^2) and normalised root-mean-
 690 square error (NRMSE) are listed for different size bins on each row. The last row concludes the overall selection of the
 691 approach model with the best configuration and its corresponding evaluation metrics.

Particle size (μm)	Approach 1 (<u>FFNN-met</u>)				Approach 2 (<u>FFNN-PSD</u>)			
	Best setting	MAE (cm^{-3})	R^2	NRMSE	Best setting	MAE (cm^{-3})	R^2	NRMSE
0.012	2; 10	2640	0.499620	0.6918	2; 10	334	0.99	0.11077
0.015	2; 15	4850	0.4237	0.59868	2; 8	216	1.00	0.0310
0.021	2; 15	6120	0.38774	0.5831	2; 15	97.8	1.00	0.01436
0.027	2; 15	8470	0.41072	0.6210	1; 25	34.0	1.00	0.0032
0.037	2; 20	8240	0.46568	0.6619	2; 15	26.3	1.00	0.0024
0.049	2; 15	6610	0.48778	0.74389	2; 25	33.7	1.00	0.0049
0.066	2; 15	4690	0.4613	0.83266	2; 10	56.7	1.00	0.01325
0.088	2; 15	3040	0.5207	0.7114	2; 4	66.2	1.00	0.0183
0.12	2; 15	1810	0.52193	0.54398	2; 8	63.1	1.00	0.0210
0.15	2; 10	917	0.29836	0.49865	2; 15	72.5	0.99	0.05215
0.21	2; 6	327	0.5536	0.7101	2; 8	114	0.91	0.3142
0.37	2; 10	95.8	0.43297	0.54396	2; 20	12.9	0.99	0.0723
0.49	2; 15	12.1	0.5025	0.6138	2; 25	0.9630	1.00	0.04237
0.66	2; 15	3.03	0.5824	0.56580	2; 15	0.1995	1.00	0.0290
0.88	2; 15	5.65	0.62190	1.4301	2; 10	0.2202	1.00	0.040398
1.17	2; 15	1.43	0.5331	0.8134	2; 8	0.0680	1.00	0.02657
1.56	2; 20	1.44	0.54384	0.81088	2; 8	0.0816	1.00	0.0312
2.08	2; 15	1.84	0.49885	0.9748	2; 8	0.0825	1.00	0.02878
2.77	2; 15	1.02	0.44352	1.0925	1; 4	0.0573	1.00	0.0372
3.70	2; 15	0.52	0.41076	1.0719	1; 8	0.0329	1.00	0.04655
4.92	2; 15	0.28	0.4427	10.009955	1; 4	0.0254	1.00	0.0681
6.56	2; 9	0.11	0.4231	0.9710	1; 6	0.0206	0.99	0.13252
8.75	2; 10	0.060	0.3903	0.9546	2; 6	0.0169	0.98	0.201980
overall	2; 15	2120	0.67	1.1324	2; 10	76.6	0.999	0.0671

692

693

Formatted: Font: 10 pt, Not Italic

710

711 Table 4. Table showing the comparison of different estimation methods, including unconditional mean (UM, column 2),
 712 median (MD, column 3), linear interpolation (LinI, column 4), logarithmic interpolation (LogI, column 5), next neighbour
 713 interpolation (nNI, column 6), previous neighbour interpolation (pNI, column 7), conditional mean by regression of
 714 meteorological parameters and other particle size number concentrations as inputs (CM – met and CM – PSD, column 8
 715 and 9, respectively) and the feed-forward neural network with meteorological parameters and other particle size number
 716 concentrations as inputs (FFNN – met and FFNN – PSD, column 10 and 11, respectively). The normalised root-mean-
 717 square error (NRMSE) of each method are listed for different size bins on each row. The last row concludes the overall
 718 evaluation metrics.

Particle size (µm)	Methods/ NRMSE									
	UM	MD	LinI	LogI	nNI	pNI	CM – met	CM – PSD	FFNN – met	FFNN – PSD
0.012	0.84	1.24	1.62	1.73	NA	1.62	0.74	0.23	0.69	0.11
0.015	0.92	1.26	0.45	0.42	0.79	0.55	0.72	0.30	0.59	0.03
0.021	0.91	1.24	0.21	0.22	0.46	0.61	0.70	0.02	0.58	0.01
0.027	1.04	1.28	0.24	0.22	0.46	0.25	0.77	0	0.62	0
0.037	1.08	1.34	0.15	0.15	0.27	0.35	0.85	0	0.66	0
0.049	1.09	1.43	0.13	0.12	0.46	0.46	0.95	0	0.74	0
0.066	1.04	1.50	0.23	0.18	0.66	0.49	1.04	0.01	0.83	0.01
0.088	0.84	1.42	0.16	0.13	0.65	0.61	0.96	0.02	0.71	0.02
0.12	0.59	1.25	0.22	0.16	0.86	0.80	0.74	0.03	0.54	0.02
0.15	1.59	1.13	0.66	0.53	1.64	0.96	0.58	0.10	0.49	0.05
0.21	11.6	1.61	3.7	3.24	4.93	1.53	1.26	0.85	0.71	0.31
0.37	23.8	1.42	1.35	1.12	3.12	1.06	0.70	0.22	0.54	0.07
0.49	185	14.4	4.16	3.53	7.98	1.00	0.83	0.15	0.61	0.04
0.66	672	54.5	2.42	2.32	3.62	2.79	0.82	0.17	0.56	0.03
0.88	485	39.4	2.06	2.07	2.02	2.18	2.20	1.12	1.43	0.04
1.17	1750	143	4.45	3.88	7.84	0.11	1.16	0.07	0.81	0.03
1.56	1750	143	0.19	0.22	0.11	0.46	1.16	0.05	0.81	0.03
2.08	1510	124	0.54	0.57	0.40	0.78	1.34	0.04	0.97	0.03
2.77	2880	236	0.47	0.30	1.48	0.92	1.43	0.04	1.09	0.04
3.70	5750	472	0.69	0.50	1.83	0.86	1.38	0.05	1.07	0.05
4.92	11000	902	0.51	0.34	1.64	1.02	1.32	0.09	1.00	0.07
6.56	27100	2220	1.09	0.86	2.51	0.83	1.26	0.12	0.97	0.13
8.75	52600	4320	4.95	3.33	1.62	NA	1.2	0.21	0.95	0.20
overall	1.95	2.23	0.58	0.57	0.88	0.88	1.39	0.17	1.13	0.07

719 Table showing the comparison of different estimation methods, including unconditional mean (UM, column 2), linear
 720 interpolation (LinI, column 3), logarithmic interpolation (LogI, column 4), next neighbour interpolation (nNI, column 5),
 721 previous neighbour interpolation (pNI, column 6), conditional mean by regression of meteorological parameters and other
 722 particle size number concentrations as inputs (CM – met and CM – PSD, column 7 and 8, respectively) and the feed-
 723 forward neural network with meteorological parameters and other particle size number concentrations as inputs (FFNN
 724 – met and FFNN – PSD, column 9 and 10, respectively). The normalised root-mean square error (NRMSE) of each
 725 method are listed for different size bins on each row. The last row concludes the overall evaluation metrics.

Particle size (µm)	Methods									
	UM	MD	LinI	LogI	nNI	pNI	CM – met	CM – PSD	FFNN – met	FFNN – PSD
0.012	0.84	1.24	1.62	1.73	NaN	1.62	0.74	0.23	0.69	0.11
0.015	0.92	1.26	0.45	0.42	0.79	0.55	0.72	0.3	0.59	0.031

0.021	0.91	1.24	0.21	0.22	0.46	0.61	0.7	0.02	0.58	0.014
0.027	1.04	1.28	0.24	0.22	0.46	0.25	0.77	0	0.62	0.0032
0.037	1.08	1.34	0.15	0.15	0.27	0.35	0.85	0	0.66	0.0024
0.049	1.09	1.43	0.13	0.12	0.46	0.46	0.95	0	0.74	0.0049
0.066	1.04	1.5	0.23	0.18	0.66	0.49	1.04	0.01	0.83	0.013
0.088	0.84	1.42	0.16	0.13	0.65	0.61	0.96	0.02	0.71	0.018
0.12	0.59	1.25	0.22	0.16	0.86	0.8	0.74	0.03	0.54	0.021
0.15	1.59	1.13	0.66	0.53	1.64	0.96	0.58	0.1	0.49	0.052
0.21	11.6	1.61	3.7	3.24	4.93	1.53	1.26	0.85	0.71	0.31
0.37	23.84	1.42	1.35	1.12	3.12	1.06	0.7	0.22	0.54	0.072
0.49	184.81	14.39	4.16	3.53	7.98	1	0.83	0.15	0.61	0.043
0.66	671.56	54.48	2.42	2.32	3.62	2.79	0.82	0.17	0.56	0.029
0.88	484.97	39.38	2.06	2.07	2.02	2.18	2.2	1.12	1.43	0.040
1.17	1749.22	143.06	4.45	3.88	7.84	0.11	1.16	0.07	0.81	0.026
1.56	1752.85	143.35	0.19	0.22	0.11	0.46	1.16	0.05	0.81	0.031
2.08	1513.46	123.72	0.54	0.57	0.4	0.78	1.34	0.04	0.97	0.028
2.77	2882.01	236.1	0.47	0.3	1.48	0.92	1.43	0.04	1.09	0.037
3.70	5753.5	471.87	0.69	0.5	1.83	0.86	1.38	0.05	1.07	0.046
4.92	$\frac{10993.5}{3}$	902.11	0.51	0.34	1.64	1.02	1.32	0.09	1.00	0.068
6.56	$\frac{27068.6}{5}$	2222.03	1.09	0.86	2.51	0.83	1.26	0.12	0.97	0.13
8.75	$\frac{52562.0}{2}$	4315.29	4.95	3.33	1.62	NaN	1.2	0.21	0.95	0.20
overall	1.95	2.23	0.58	0.57	0.88	0.88	1.39	0.17	1.13	0.067